EPM/RT-92-6

ROTOR-STATOR PASSAGE-AVERAGED SIMULATION WITHIN A MIXED-FLOW PUMP

Xudong Zhang, Research Assistant
André Garon, Research Fellow
Ricardo Camarero, Professor

Génie Mécanique

École Polytechnique de Montréal
avril 1992

Ce document a pu être publié grâce à une subvention du Conseil de recherches en sciences et en génie du Canada (CRSNG)

Dépôt légal, 2e trimestre 1992
Bibliothèque nationale du Québec
Bibliothèque nationale du Canada

Pour se procurer une copie de ce document, s'adresser au:

Service de l'édition
École Polytechnique de Montréal
Case postale 6079, Succursale A
Montréal (Québec) H3C 3A7
(514) 340-4000

Compter 0,10$ par page (arrondir au dollar le plus près) et ajouter 3,00$ (Canada) pour la couverture, les frais de poste et la manutention. Régler en dollars canadiens par chèque ou mandat-poste au nom de l'École Polytechnique de Montréal. Nous n'honorerons que les commandes accompagnées d'un paiement, sauf s'il y a eu entente préalable dans le cas d'établissements d'enseignement, de sociétés ou d'organismes canadiens.

ROTOR-STATOR PASSAGE-AVERAGED SIMULATION WITHIN A MIXED-FLOW PUMP

Xudong Zhang* André Garon† Ricardo Camarero‡
École Polytechnique de Montréal, C.P. 6079, Succ. A,
Montréal, Québec, Canada, H3C 3A7

Abstract

A methodology for the simulation of the rotor-stator flow interaction is presented. This is based on a the three-dimensional closure of the passage-averaged vorticity-potential formulation of the flow field in such configurations. A three-dimensional solver and a passage-averaged solver are used sequentially in the algorithm. These solvers were tested individually and then as a whole. Finally, the methodology is applied to the simulation of the flow within a mixed-flow pump and comparison with experimental results are presented.

1 Introduction

The flow in a single stage turbomachine owes its complexity to the three-dimensional flow exiting from the stator and interacting with a moving rotor. This flow field is unsteady, spatially aperiodic and highly rotational, making the

*Research Assistant

†Research Fellow

‡Professor

coupling between the stator and rotor flows in a turbomachine an extremely difficult problem to solve.

From the numerical methods and computing systems points of view, the resolution of the full equations of motion for a multistage turbomachine is a formidable if not impossible task. To achieve practical numerical simulations within current computational capabilities, appropriate modelling and approximations is required to simplify the governing set of equations.

The passage-averaged representation is obtained by integrating the flow equations in the circumferential direction of the blade row. This means that the passage-averaged flow properties are defined on the average meridional cross-section of the turbomachine. If the flow is assumed to be periodic from one blade passage to another, the passage-averaged flow properties can be represented by integration from the pressure side to suction side of the blade. In the derived formulations, a tangential blockage parameter, which is a geometrical factor, is introduced to replace the flow dependent streamsheet thickness in the stream-surface formulations. Details about the through-flow approach is reviewed in Hirsch & Deconinck (1985).

In this class of approximation, the blade-to-blade effects are replaced by external forces which are coupled to the through-flow governing equations. To evaluate these external forces, a closure model must be developed. This approximation was initially proposed by Bosman & Marsh (1974) for applications in through-flow calculations and subsequently used by Bosman & El-Shaarawi (1977) and Jennions & Stow (1985a,1985b). Based on the same principle, a more elaborate model has been developed by Adamczyk (1984) and applied to the full three-dimensional model. This approximation has shown its advantages and its flexibility to simulate flows through multistage turbomachines but requires computer resources not commonly available.

The objectives of this paper are twofold: first to simulate the rotor-stator flow interaction within a single stage turbomachine and second to test and evaluate the capability of the vorticity-potential formulation to achieve this task.

2 Computational Method

2.1 Governing Equations

The governing equations used in this study are based on the vorticity, scalar potential and vector potential formulation of the Navier-Stokes equations, which can be written as follows

$$(\mathbf{V}\cdot\nabla)\mathbf{W} - (\mathbf{W}\cdot\nabla)\mathbf{V} = \frac{1}{Re}\nabla^2\mathbf{W} \tag{1}$$

$$\nabla^2\phi = 0 \tag{2}$$

$$\nabla^2\mathbf{A} = -\mathbf{W} \tag{3}$$

$$\mathbf{V} = -\nabla\phi + \nabla\times\mathbf{A} \tag{4}$$

where $\mathbf{V} = (v^r,\ v^\theta,\ v^z)$, $\mathbf{W} = (w^r,\ w^\theta,\ w^z)$ and $\mathbf{A} = (A^r,\ A^\theta,\ A^z)$, in cylindrical coordinates $(r,\ \theta,\ z)$, are the velocity, vorticity and vector potential fields respectively, ϕ is the scalar potential and Re is the Reynolds number.

These three-dimensional equations can be integrated along the circumferential direction from pressure side to suction side of the blade passages to yield the passage-averaged form of the governing equations. The passage-averaged vorticity transport equation, the two potential equations, and the swirl equation together with the velocity expression form a complete set of equations for the through-flow computation. These equations are expressed below and are called the modified passage-averaged equations

$$\begin{aligned}\bar{v}^r\frac{\partial}{\partial r}(B\bar{w}^\theta) &+ \bar{v}^z\frac{\partial}{\partial z}(B\bar{w}^\theta) - \frac{\bar{v}^r}{r}(B\bar{w}^\theta) - \frac{1}{r}\frac{\partial}{\partial z}(B\bar{v}^\theta\bar{v}^\theta)\\ &= \frac{1}{Re}\{\frac{\partial}{\partial r}[\frac{1}{r}\frac{\partial}{\partial r}(rB\bar{w}^\theta)] + \frac{\partial^2}{\partial z^2}(B\bar{w}^\theta)\} + F_w^\theta\end{aligned} \tag{5}$$

$$\frac{1}{r}\frac{\partial}{\partial r}[r\frac{\partial}{\partial r}(B\bar{\phi})] + \frac{\partial^2}{\partial z^2}(B\bar{\phi}) = F_\phi \tag{6}$$

$$\frac{\partial}{\partial r}[\frac{1}{r}\frac{\partial}{\partial r}(B\bar{A}^\theta)] + \frac{\partial^2}{\partial z^2}(B\bar{A}^\theta) = -B\bar{W}^\theta + F_A^\theta \tag{7}$$

$$\bar{v}^r\frac{\partial}{\partial r}(B\bar{v}^\theta) + \bar{v}^z\frac{\partial}{\partial z}(B\bar{v}^\theta) + \frac{\bar{v}^r}{r}(B\bar{v}^\theta) = \frac{1}{Re}\{\frac{\partial}{\partial r}[\frac{1}{r}\frac{\partial}{\partial r}(rB\bar{v}^\theta)] + \frac{\partial^2}{\partial z^2}(B\bar{v}^\theta)\} + F_v^\theta \tag{8}$$

where

$$B\bar{v}^r = -\frac{\partial B\bar{\phi}}{\partial r} - \frac{\partial(B\bar{A}^\theta)}{\partial z} + F_v^r \tag{9}$$

$$B\bar{v}^z = -\frac{\partial B\bar{\phi}}{\partial z} + \frac{\partial(B\bar{A}^\theta)}{\partial r} + \frac{1}{r}(B\bar{A}^\theta) + F_v^z \tag{10}$$

the over bar " - " represents the passage-averaged variables, and F_w^θ, F_ϕ, F_A^θ, F_v^θ, F_v^r and F_v^z are external forces resulting from integrations and are given in Appendix I for completeness. B is the blockage factor defined by

$$B = \frac{N(\theta_s - \theta_p)}{2\pi} \tag{11}$$

in which N represents the blade number.

2.2 Boundary Conditions

To obtain a unique scalar and vector potentials, a set of compatible restrictions on the potentials must be imposed. Discussions about the admissible boundary conditions for the potentials can be found in the work of Hirasaki & Hellums (1970), Richardson & Cornish (1977) and Yang & Camarero (1991)

The boundary conditions used for the three-dimensional equations are summarized in Table 1 in which v_n^i, v_n^o are the mean normal inlet and outlet velocities and $\mathbf{E}$ is a vector defined on the inlet surface S that satisfies

$$\mathbf{E}\cdot\mathbf{t}_1 = 0, \quad \mathbf{E}\cdot\mathbf{t}_2 = 0, \quad \mathbf{n}\cdot[(\nabla_s \times (\nabla_s \times \mathbf{E})] = \mathbf{n}\cdot\mathbf{V} - v_n^i \tag{12}$$

In these equations, $\{\mathbf{n}, \mathbf{t}_1, \mathbf{t}_2\}$ is a local orthogonal coordinate system.

The boundary conditions for the modified passage-averaged equations are summarized in Table 2 in which $\bar{v}_n^i$ and $\bar{v}_n^o$ are the average normal inlet and outlet velocities respectively.

2.3 Solution Procedure

The proposed methodology for the simulation of the rotor-stator flow interaction consists in the coupling of two sets of governing equations; the three-dimensional governing equations (3DGE) and the modified passage-averaged governing equations (MPAGE). The 3DGE are used within each blade region to provide the three-dimensional flow fields, while the MPAGE are used to link in an average sense these flow fields. Outside the blade passages, the flow is taken to be axisymmetric. Within the blade passages, the presence of the blades are accounted for by force terms whose expressions are deduced from the 3DGE solutions. All these terms can be computed explicitly and the calculations can be performed outside the 3DGE and MPAGE solvers. The input data are the geometry parameters and the 3DGE solutions. The output data are the external force terms which are needed for solving the MPAGE.

From the formulation of the 3DGE, it is clear that in order to solve these equations, the only required information is the inlet velocity distribution. In the present study, since the flow is taken to be axisymmetric outside the blade rows, the inflow conditions at the entrance of each blade row are the passage-averaged velocity profile. These inlet velocities are updated by the MPAGE solutions.

In summary, the data flow from the 3DGE to the MPAGE and vice versa is repeated until convergence is achieved.

3 Calculation Results

3.1 Validations

The proposed model for the rotor-stator interactions in a turbomachine, and the resulting governing equations, the 3DGE and the MPAGE, have been implemented in a Fortran computer program. To validate this approach, numerical results for several simple flow problems are presented, and the numerical predictions are compared with available analytical or experimental results.

Developing Flow in a Straight duct

The development of a laminar flow in a rectangular duct is a simple three-dimensional internal flow for which analytical solutions and experimental results are available for comparison. The flow in the duct geometry, illustrated in Figure 1, with aspect ratio $\gamma = b/a = 1$, i.e. with square cross section, was first computed. Constant spacing was used in the x- and y-directions, with 15x15 points, and 23 points were stretched in the streamwise z-direction. The Reynolds number, based on the hydraulic diameter D_h was chosen to be $Re = 100$. Based on the work of Han (1960), the duct length L was set to

$$L = 0.105\, D_h\, Re \tag{13}$$

to ensure a fully developed flow at the exit. On the inlet plane, a uniform flow was specified with $v^x = v^y = 0$, and $v^z = 1$ (note that v^z is set to zero at the walls to satisfy the no-slip condition).

The predicted velocity distributions along the central plane in the developing region are shown in Figure 2a at several sections. Figure 2b shows the velocity profiles taken along the duct diagonal, i.e. with the coordinates x=y. These velocity profiles are compared with the analytical solution of Han (1960) and

with the experimental data of Goldstein & Kreid (1967). Very good agreement can be observed in these figures.

Also the predicted fully developed streamwise velocity profiles (Figure 3), and the centerline velocity development (Figure 4) are in good agreement with the analytical solutions of Han (1960) and the experimental data of Goldstein & Kreid (1967).

Developing Flow in Curved duct

The second test problem was the development of a laminar incompressible viscous flow in a curved duct with square cross section. The principal characteristic of such a flow is the presence of longitudinal curvature which generates secondary flows resulting in distortion of the streamwise velocity. The computation of curved duct flows usually serves as a model problem for understanding some of the important features in turbomachinery flows.

The duct geometry is illustrated in Figure 5. The centerline curvature R_c of the curved duct is 14 times the duct width D. The Dean number is 55 corresponding to a Reynolds number of 206, based on the hydraulic diameter D_h, and the turning angle is 110°. On a transverse cross section, 15 points are uniformly spaced in the radial direction and 13 on the width and 25 points were stretched in the streamwise direction. At the entrance of the duct, a uniform streamwise velocity profile and zero transverse velocities were specified.

Figure 6 shows the development of the streamwise velocity profiles in the mid-plane parallel to the top and bottom walls. The profiles in Figure 6b, along the vertical direction, remain symmetric as they should on the vertical mid-surface. The profiles in Figure 6a, along the horizontal direction, become more asymmetric as the flow develops downstream. This can be explained by the centrifugal force generated by the longitudinal curvature which forces the peak

value of the velocity profile towards the outer wall of the duct.

In Figure 7, the predicted velocity profiles at the cross section with angular position $\theta = 102.4^o$ are chosen for comparison with the fully developed flow predicted by Ghia & Sokhey (1977) and Cheng et al. (1975), and with the experimental data of Mori et al. (1971). The present calculations and the previous numerical predictions agree very well while the comparison between the numerical results and experimental data disagree somewhat.

Flow in a Rectangular Duct

The geometry of the first test problem is now used in this test to validate the MPAGE. The passage-averaging technique has been applied to the analytical solution of Han (1960) which results in the analytical averaged solution of the velocity for comparison with the computed averaged solutions. Their expression are given in Appendix *II*. The Reynolds number, based on the inlet velocity and the hydraulic diameter D_h, is $Re = 100$ for these tests. The computations were carried out using three uniformly spaced grids, 15x15x31, 15x13x31 and 15x11x31, with aspect ratios $\gamma = 1.0$, 0.5 and 0.25 respectively. The profiles of the passage-average velocities are presented at several sections (Figure 8). Good agreement for all aspect ratios can be observed in this figure.

3.2 Mixed-Flow Pump

Description of the NEL Pump

The NEL pump is a mixed-flow machine with a five blades rotor and a nine blades stator. Details of the physical dimensions of the blades and a general description of the pump are given in Carey et al. (1985a).

The measurements reported by Carey et al. (1985b) were performed in an air model of the machine at a shaft speed 1200 r.p.m. of the rotor. The experimental

data for all velocities are normalized by the blade velocity at the rotor trailing edge midpoint, which is $U_t = 27m/s$, corresponding to a Reynolds number of Re=1.5x10^6. However, since the present study is for laminar flow, the Reynolds number for the numerical computation, run at the best efficiency point of the pump, was set to 1500.

The meridional computational domain is shown in Figure 9, which is divided into five regions. The rotor is located from $s = 1$ to $s = 2$ and the stator from $s = 3$ to $s = 4$. The inlet is at station $s = 0$ and the outlet at $s = 5$. It is noted that in the numerical simulation, the rotor tip clearance was not considered.

A grid of 13x59 was used for the MPAGE computation with 13 points in the radial direction. There were 15 points spaced uniformly in the circumferential direction for the rotor and 13 points for the stator.

Rotor Three-Dimensional Results

For comparison of the numerical predictions with the experimental measurement of Carey et al. (1985b), the results are presented in terms of the velocity component parallel to the streamwise grid line, V_p, the tangential velocity component in the relative rotating frame of reference, W_t and the velocity component normal to the streamwise grid line, V_n.

Figures 10 to 12 show the blade-to-blade velocity variations from the suction side "SS" to the pressure side "PS" and from hub-to-shroud. Also to show, in these figures, the streamwise evolutions of the velocity components within the rotor, the blade-to-blade variations are given near the rotor inlet (s=1.07), at mid-chord (s=1.5) and near the rotor outlet (s=1.87). On these figures, the blade-to-blade graphs are numbered from 3 to 12 corresponding to the normalized hub-to-shroud distance R=0.167, 0.333, 0.5, 0.667, 0.833 as 0.917 and detailed in Carey et al. (1985b).

Due to the change of the rotor geometry, the velocity component V_p (Figure 10) is accelerated near the blade suction surface in the mainstream flow region (R < 0.833). In the same region, the relative tangential component W_t (Figure 11) is decelerated near the suction surface and accelerated near the pressure surface. These observations agree well with the experimental data except at the edge of the blade surface boundary layers, where, the velocities are relatively higher than the measured ones. This is as be expected since the Reynolds number for the computation is a thousand times lower than the experimental one. Consequently, a thicker boundary layer on the blade surface is observed which induces higher velocities at the edge of the boundary layer.

In the near shroud region, 0.833 < R < 1.0, complex turbomachinery flow phenomena are encountered. The blade boundary layers, the shroud boundary layer, the effects of the relative motion of the shroud and the associated secondary flow interacts to generate rapid changes in the fluid behaviour. It is evident that there is a discrepancy between the predictions and the measurements for velocity components V_p and W_t shown in Figures 10 and 11.

The main reason for such a discrepancy is probably the absence of the blade-tip gap in the present numerical modeling. When the flow proceeds downstream, the tip leakage flow meet and interact with blade and shroud boundary layers, giving rise to a mixing region. Without the tip leakage flow, the shroud boundary layer will play an important role in the outer annular region. Indeed, the numerical predictions in Figures 10 and 11 show that, the flow close to the suction surface is decelerated, while near the pressure surface, the flow is accelerated by the moving shroud.

Stator Three-Dimensional Results

Like the rotor, the results of the stator are plotted in terms of the same velocity components V_p, V_t and V_n, where V_t represents the absolute tangential velocity component.

From Figures 13 through 15, one can see that the boundary layer development in the stator passage, for both blade surfaces and the end-walls, is more significant than in the rotor passage, as the passage of the stator is much longer than that of the rotor. Because of the conically inward shaped hub and shroud and the presence of the pressure surface of the blade, the mainstream flow develops toward the region near the pressure surface as shown in Figure 13. When the flow proceeds downstream, velocity component V_P is accelerated in the region near the pressure surface, but decelerated in the region near the suction surface.

Another important feature of the flow in the stator is that, as shown in Figure 14, the tangential velocity V_t is reduced very rapidly along the passage. Near the hub and exit region, the tangential velocity even becomes positive. This behavior is as expected, since the function of a diffuser (the stator in the present pump model) is to reduce the high velocity in order to convert the kinetic energy into static pressure. Although a quantitative comparison with measurement is not available, the revealed flow features by the numerical prediction are reasonable and quite encouraging.

From Figure 15, one can observe that, as the flow develops downstream, V_n exhibits an outward flow towards the suction side of the passage, and an inward flow towards the pressure side indicating the presence of secondary flows within the stator passage.

MPAGE Results without Stator

It is interesting to conduct a test for the performance of the stator. This can be done by imposing all the external force terms to zero within the stator passage while keeping them within the rotor passage. In other words, the presence of the stator is totally neglected. For this pump, the function of the stator is to convert kinetic energy into pressure. Since the flow is incompressible, this energy is taken from the swirl component, W_t, of the velocity field generated by the rotor. In the absence of the stator, W_t, at the exit, is expected to be larger than with the stator. Indeed, this result is supported by the present numerical prediction shown in Figure 16. It is observed that the velocity component V_p has no significant change (since the flow must conserve the mass across the blade section), while the velocity component W_t is dramatically decreased by the presence of the stator as the flow develops downstream.

4 Conclusions

The passage-averaged and the three-dimensional vorticity-potential formulations have been used sequentially in a numerical procedure to simulate the rotor-stator flow interaction. In the passage-averaged equations, the presence of the blades is accounted for by force terms whose values are deduced from the three-dimensional flow fields. This procedure requires some iterations between the passage-averaged solutions and the three-dimensional solutions to achieve a convergent flow field. With regard to computer resources, this approach has many advantages:

(i) It avoids a full three-dimensional time dependent computation through a complete turbomachine.

(ii) It does not require the interpolation between the rotor moving grid and

the stator stationary grid.

(iii) The external forces from the three-dimensional computations are more accurate than the forces from an approximate blade-to-blade computation.

(iv) It links the three-dimensional flow fields of the rotor and stator in an averaged sense.

The numerical procedure have been thoroughly validated with analytical and experimental data when available. The validation were performed on each set of equations individually, 3DGE and MPAGE, and as a whole. The proposed model also has been applied to a mixed-flow pump and the predicted solution were compared with experimental data. However, because no measurement were available for the stator, no quantitative conclusion can be drawn about the predictive capability of the stator.

5 Acknowledgments

This work was supported by the National Science and Engineering Research Council of Canada (NSERC) and by the Centre de Recherche Informatique de Montréal (CRIM) and Institut de Recherche et Etude du Hydro-Québec (IREQ).

References

1. Adamczyk,J.J. (1984), Model equation for simulating flows in multistage turbomachinery, NASA TM 86869.

2. Bosman,C. and El Shaarawi,M.A.I. (1977), Quasi three-dimensional numerical solution of flow in turbomachines, J. Fluid Eng., ASME, 99, pp.132-140.

3. Bosman,C. and Marsh,H. (1974), An improved method for calculating the flow in turbomachines including a consistent loss model, J. Mech. Eng.

Sci., 16, pp.25-31

4. Carey,C., Fraser,S.M., Rachman,D. and Wilson,G. (1985a), Studies of the flow of air in a model mixed-flow pump using laser doppler anemometry, Part 1: Research facility and instrumentation, NEL Report 698.

5. Carey,C., Fraser,S.M., Rachman,D. and Wilson,G. (1985b), Studies of the flow of air in a model mixed-flow pump using laser doppler anemometry, Part 2: Velocity measurements within the impeller, NEL Report 699.

6. Cheng,K.C., Lin,R.C. and Ou J.W. (1976), Fully developed laminar flow in curved rectangular channels, J. Fluids Eng., ASME, 98, pp.41-48.

7. Ghia,K.N. and Sokhey,J.S. (1977), Laminar incompressible viscous flow in curved ducts of regular cross-sections, J. Fluids Eng., 99, pp.640-648.

8. Goldstein,R.J. and Kreid,D.K. (1967), Measurement of laminar flow development in a square duct using a laser-doppler flowmeter, J. Appl. Mech., ASME, 34, pp.813-818.

9. Han,L.S. (1960), Hydrodynamic entrance lengths for incompressible laminar flow in rectangular ducts, J. Appl. Mech., ASME, 27, pp.403-409.

10. Hirasaki,G.J. and Hellums,J.D. (1970), Boundary conditions on the vector and scalar potentials in viscous three-dimensional hydrodynamics, Quart. Appl. Math., 28, pp.293-296.

11. Hirsch,Ch. and Deconinck,H. (1985) Through flow models in turbomachines: Stream surface and passage average equation representation, Thermodynamics and Fluid Mechanics of Turbomachinery, 1, pp.73-129.

12. Jennions,I.K. and Stow,P. (1985a), A Quasi-three-dimensional turbomachinery blade design system: Part I - Throughflow analysis, J. Eng. Gas

Turbines and power, ASME, 107, pp.301-307.

13. Jennions,I.K. and Stow,P. (1985b), A Quasi-three-dimensional turbomachinery blade design system: Part II - Computerized system, J. Gas Turbines and power, ASME, 107, pp.308-316.

14. Mori,Y., Uchida,Y. and Ukon,T. (1971), Forced convection heat transfer in a curved channel with a square cross section, Int. J. Heat Mass Transfer, 14, pp.1787-1805.

15. Richardson,S.M. and Cornish,A.R.H. (1977), Solution of three-dimensional incompressible flow problems, J. Fluid Mech., 82, pp.309-319.

16. Sparrow,E.M., Hixon,C.W. and Shavit,G. (1967), Experiments on laminar flow development in rectangular ducts, J. Basic Eng., ASME, 89, pp.116-124.

17. Yang H.R. and Camarero R. (1991), Internal three-dimensional viscous flow solutions using the vorticity-potential method, Int. J. Numer. Meth. Fluids, 12, pp.1-15.

Appendix I

The External forces for the modified passage-averaged equations are

$$
\begin{aligned}
F_w^\theta \;=\; & \frac{1}{Re\;k}\quad [\frac{1}{r}\frac{\partial}{\partial\theta}(\nabla\lambda_s\cdot\mathbf{W}_s-\nabla\lambda_p\cdot\mathbf{W}_p)] \\
& -[\frac{\partial}{\partial z}(\frac{1}{r}(\frac{\partial\lambda_s}{\partial\theta}w_s^z-\frac{\partial\lambda_p}{\partial\theta}w_p^z)-(\frac{\partial\lambda_s}{\partial\theta}w_s^\theta-\frac{\partial\lambda_p}{\partial\theta}w_p^\theta)) \\
& -\frac{\partial}{\partial r}((\frac{\partial\lambda_s}{\partial r}w_s^\theta-\frac{\partial\lambda_p}{\partial r}w_p^\theta)-\frac{1}{r}(\frac{\partial\lambda_s}{\partial\theta}w_s^r-\frac{\partial\lambda_p}{\partial\theta}w_p^r))] \\
& -[(\frac{\partial\lambda_s}{\partial z}(\frac{1}{r}\frac{\partial w^z}{\partial\theta}-\frac{\partial w^\theta}{\partial z})_s-\frac{\partial\lambda_p}{\partial z}(\frac{1}{r}\frac{\partial w^z}{\partial\theta}-\frac{\partial w^\theta}{\partial z})_p) \\
& -(\frac{\partial\lambda_s}{\partial r}(\frac{1}{r}w^\theta-\frac{\partial w^\theta}{\partial r}-\frac{1}{r}\frac{\partial w^r}{\partial\theta})_s \\
& -\frac{\partial\lambda_p}{\partial r}(\frac{1}{r}w^\theta-\frac{\partial w^\theta}{\partial r}-\frac{1}{r}\frac{\partial w^r}{\partial\theta})_p)] \\
& -\frac{1}{k}\quad {}^n\bar{v}^\theta[\nabla\lambda_s\cdot\mathbf{W}_s-\nabla\lambda_p\cdot\mathbf{W}_p] \\
& -r\omega[(\frac{\partial\lambda_s}{\partial z}w_s^z-\frac{\partial\lambda_p}{\partial z}w_p^z)+(\frac{\partial\lambda_s}{\partial r}w_s^r-\frac{\partial\lambda_p}{\partial r}w_p^r)] \\
& -\quad \frac{\partial}{\partial z}(B\overline{\tilde{w}^\theta\tilde{v}^z}-B\overline{\tilde{w}^z\tilde{v}^\theta})-\frac{\partial}{\partial r}(B\overline{\tilde{w}^r\tilde{v}^\theta}-B\overline{\tilde{w}^\theta\tilde{v}^r}) \\
& -\bar{w}^\theta[\frac{\partial B}{\partial r}\bar{v}^r+\frac{\partial B}{\partial z}\bar{v}^z] \\
& +\quad [\frac{\partial(B\bar{v}^\theta)}{\partial r}+\frac{1}{r}B\bar{v}^\theta-\frac{r\omega}{k}(\frac{\partial\lambda_s}{\partial z}-\frac{\partial\lambda_p}{\partial z})]\frac{\partial\bar{v}^\theta}{\partial z} \\
& -[\frac{\partial(B\bar{v}^\theta)}{\partial z}+\frac{r\omega}{k}(\frac{\partial\lambda_s}{\partial z}-\frac{\partial\lambda_p}{\partial z})]\frac{\partial\bar{v}^\theta}{\partial r} \\
& +\frac{r\omega}{k}(\frac{\partial\lambda_s}{\partial z}-\frac{\partial\lambda_p}{\partial z})(\frac{1}{r}\bar{v}^\theta)
\end{aligned}
\tag{14}
$$

$$
\begin{aligned}
F_A^\theta \;=\; & -\frac{1}{k}\quad [\frac{1}{r}\frac{\partial}{\partial\theta}(\nabla\lambda_s\cdot\mathbf{A}_s-\nabla\lambda_p\cdot\mathbf{A}_p)] \\
& +[(\frac{\partial\lambda_s}{\partial z}(\frac{1}{r}\frac{\partial A^z}{\partial\theta}-\frac{\partial A^\theta}{\partial z})_s-\frac{\partial\lambda_p}{\partial z}(\frac{1}{r}\frac{\partial A^z}{\partial\theta}-\frac{\partial A^\theta}{\partial z})_p] \\
& -[\frac{\partial\lambda_s}{\partial r}(\frac{1}{r}A^\theta-\frac{\partial A^\theta}{\partial r}-\frac{1}{r}\frac{\partial A^r}{\partial\theta})_s \\
& -\frac{\partial\lambda_p}{\partial r}(\frac{1}{r}A^\theta-\frac{\partial A^\theta}{\partial r}-\frac{1}{r}\frac{\partial A^r}{\partial\theta})_p]
\end{aligned}
\tag{15}
$$

$$
\begin{aligned}
F_v^\theta \;=\; \frac{1}{Re\ k}\;\Big(\;
&[\frac{\partial\lambda_s}{\partial r}((\frac{\partial v^\theta}{\partial r})_s-\frac{1}{r}v_s^\theta)-\frac{\partial\lambda_s}{\partial r}((\frac{\partial v^\theta}{\partial r})_s-\frac{1}{r}v_s^\theta)]\\
&+\frac{1}{r}[\frac{\partial\lambda_s}{\partial\theta}(\frac{\partial v^\theta}{\partial\theta})_s-\frac{\partial\lambda_p}{\partial\theta}(\frac{\partial v^\theta}{\partial\theta})_p]\\
&+[\frac{\partial\lambda_s}{\partial z}(\frac{\partial v^\theta}{\partial z})_s-\frac{\partial\lambda_p}{\partial z}(\frac{\partial v^\theta}{\partial z})_p]\\
&+r\omega[\frac{\partial}{\partial r}(\frac{\partial\lambda_s}{\partial r}-\frac{\partial\lambda_p}{\partial r})-\frac{\partial}{\partial z}(\frac{\partial\lambda_s}{\partial z}-\frac{\partial\lambda_p}{\partial z})]\\
-\quad &\frac{2}{r}B\overline{\tilde{v}^r\tilde{v}^\theta}+\frac{\partial}{\partial r}(B\overline{\tilde{v}^r\tilde{v}^\theta})+\frac{\partial}{\partial z}(B\overline{\tilde{v}^z\tilde{v}^\theta})\\
&-\bar{v}^\theta[\frac{\partial B}{\partial r}\bar{v}^r+\frac{\partial B}{\partial z}\bar{v}^z]\quad+\quad B\overline{D_p}
\end{aligned}
\tag{16}
$$

$$
F_\phi \;=\; -\frac{1}{k}\nabla\cdot(\phi_s\nabla\lambda_s-\phi_p\nabla\lambda_p) \tag{17}
$$

$$
F_v^r \;=\; -\frac{1}{k}(\frac{\partial\lambda_s}{\partial r}\phi_s-\frac{\partial\lambda_p}{\partial r}\phi_p) \tag{18}
$$

$$
F_v^z \;=\; -\frac{1}{k}(\frac{\partial\lambda_s}{\partial z}\phi_s-\frac{\partial\lambda_p}{\partial z}\phi_p) \tag{19}
$$

with

$$
\begin{aligned}
D_p \;=\; &\frac{1}{Re}[\frac{\partial}{\partial r}(\frac{1}{r}\frac{\partial v^\theta}{\partial r})+\frac{\partial^2 v^\theta}{\partial z^2}]\\
&-[\frac{1}{r}\frac{\partial}{\partial r}(rv^rv^\theta)+\frac{\partial}{\partial z}(v^zv^\theta)+\frac{1}{r}v^rv^\theta]
\end{aligned}
\tag{20}
$$

where subscripts "s" and "p" represent the values of the variables on the suction surface and pressure surface respectively, and the tilde " ˜ " represents their perturbation from their average value.

Appendix II

From the paper of Han (1960), one can express the axial velocity to a rectangular duct (see Figure 1) as follows

$$
u_z=\frac{\pi^2}{4}C^{-1}\sum_{m,n=1}^{\infty}\frac{(-1)^{m+n}\cos[(2m-1)\pi x/2a]\cos[(2n-1)\pi y/2b]}{(2m-1)(2n-1)[(2m-1)^2\gamma^2+(2n-1)^2+(2\beta b/\pi)^2]} \tag{21}
$$

where

$$
C=\sum_{m,n=1}^{\infty}1/(2m-1)^2(2n-1)^2[(2m-1)^2\gamma^2+(2n-1)^2+(2\beta b/\pi)^2] \tag{22}
$$

The parameter β and its relations with axial distance can be found in Han (1960).

Employing the passage-averaging procedure described in section 3.2, the velocity in (21) is averaged across the y-direction and gives

$$\overline{u}_z = \frac{\pi}{2} C^{-1} \sum_{m=1}^{\infty} \frac{(-1)^{m+1}}{2m-1} D_m \cos[(2m-1)\pi x/2b] \tag{23}$$

where

$$D_m = \sum_{n=1}^{\infty} 1/(2n-1)^2[(2m-1)^2\gamma^2 + (2n-1)^2 + 2\beta b/\pi)^2] \tag{24}$$

	Solid Wall	Inlet	Outlet
ϕ	$\frac{\partial \phi}{\partial n} = 0$	$\frac{\partial \phi}{\partial n} = v_h^i$	$\frac{\partial \phi}{\partial n} = v_n^0$
$\mathbf{A}$	$\mathbf{A}_t = 0$ $\nabla \cdot \mathbf{A} = 0$	$\mathbf{A}_t = \nabla_S \times E$ $\nabla \cdot \mathbf{A} = 0$	$\frac{\partial^2 \mathbf{A}}{\partial \mathbf{s}^2} = 0$
$\mathbf{W}$	$\mathbf{W} = (\nabla \times \mathbf{V})_{\text{Wall}}$	$\mathbf{W} = (\nabla \times \mathbf{V})_{\text{Inlet}}$	$\frac{\partial \mathbf{W}}{\partial \mathbf{s}} = 0$

Table 1: Boundary Conditions for 3DGE

	Solid Wall	Inlet	Outlet
$\bar{\phi}$	$\frac{\partial \bar{\phi}}{\partial n} = 0$	$\frac{\partial \bar{\phi}}{\partial n} = \bar{v}_n^i$	$\frac{\partial \bar{\phi}}{\partial n} = \bar{v}_n^0$
$\bar{A}^\theta$	$\bar{A}^\theta = 0$	$\bar{A}^\theta = 0$	$\frac{\partial^2}{\partial s^2}(B\bar{A}^\theta) = 0$
$\bar{w}^\theta$	$B\bar{w}^\theta = \frac{\partial (B\bar{v}^r)}{\partial z} - \frac{\partial (B\bar{v}^z)}{\partial r}$	$B\bar{w}^\theta = \frac{\partial (B\bar{v}^r)}{\partial z} - \frac{\partial (B\bar{v}^z)}{\partial r}$	$\frac{\partial}{\partial s}(B\bar{w}^\theta) = 0$
$\bar{v}^\theta$	$\bar{v}^\theta = (\bar{v}^\theta)_{\text{wall}}$	$\bar{v}^\theta = \bar{v}_i^\theta$	$\frac{\partial}{\partial s}(B\bar{v}^\theta) = 0$

Table 2: Boundary Conditions for MPAGE

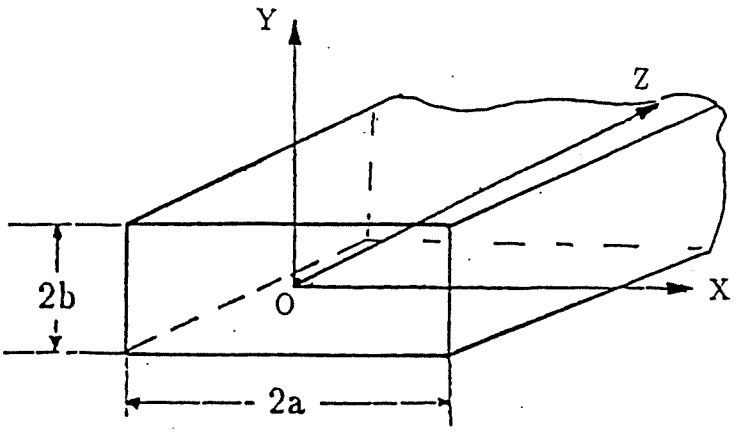

Figure 1: Duct Configuration

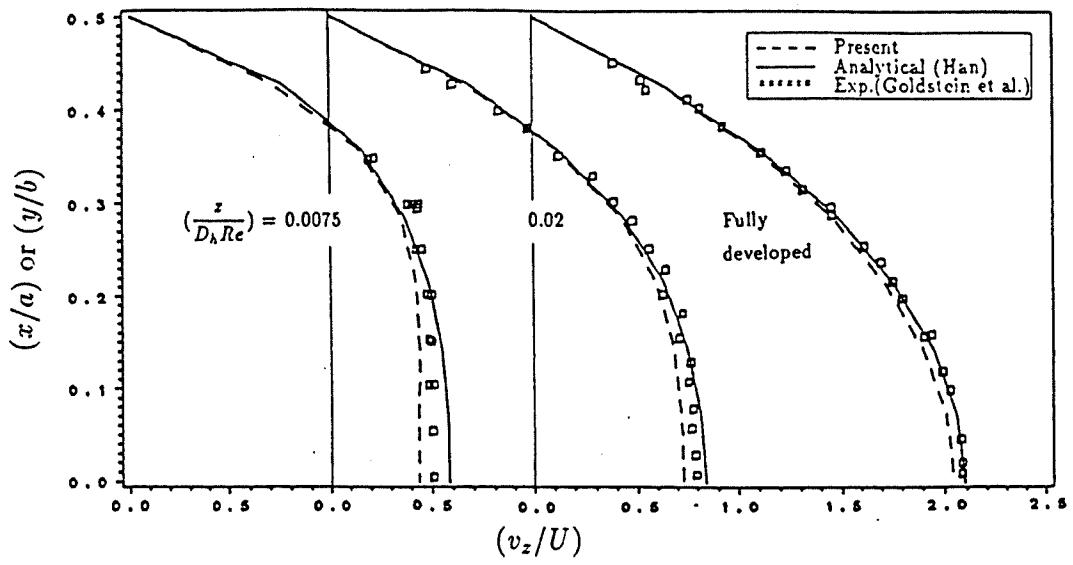

(a) Central plane

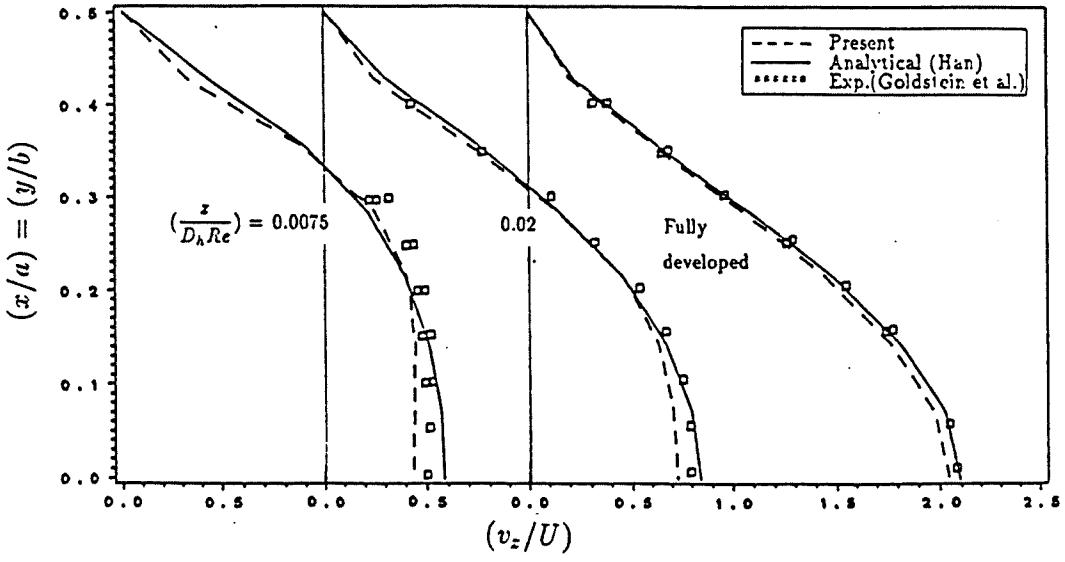

(b) Diagonal plane

Figure 2: Velocity Development for a Straight Duct with Aspect Ratio $\gamma = 1.0$

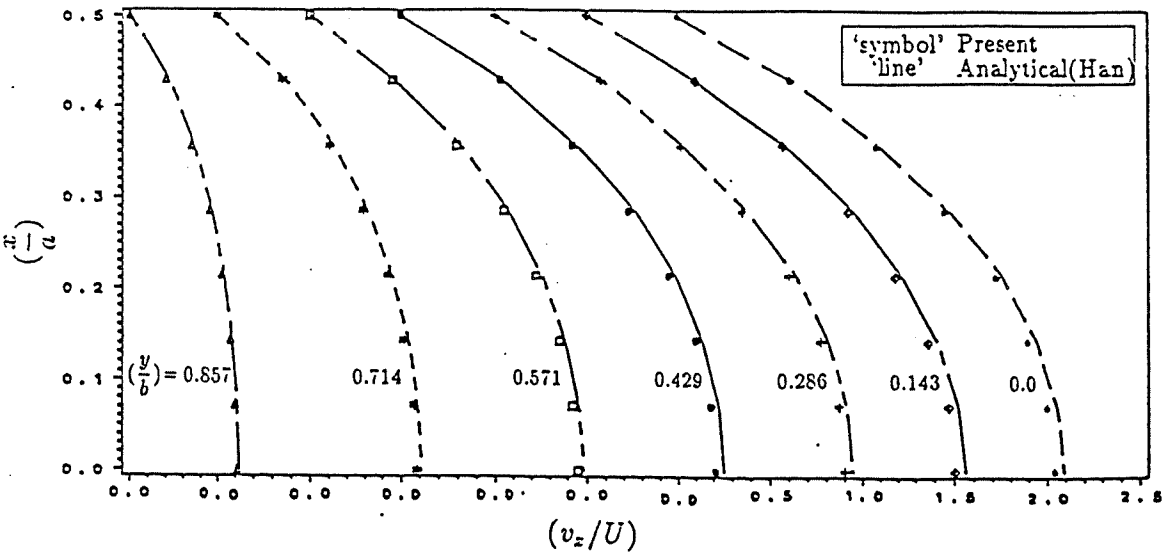

Figure 3: Fully-Developed Velocity Profiles, $\gamma = 1.0$

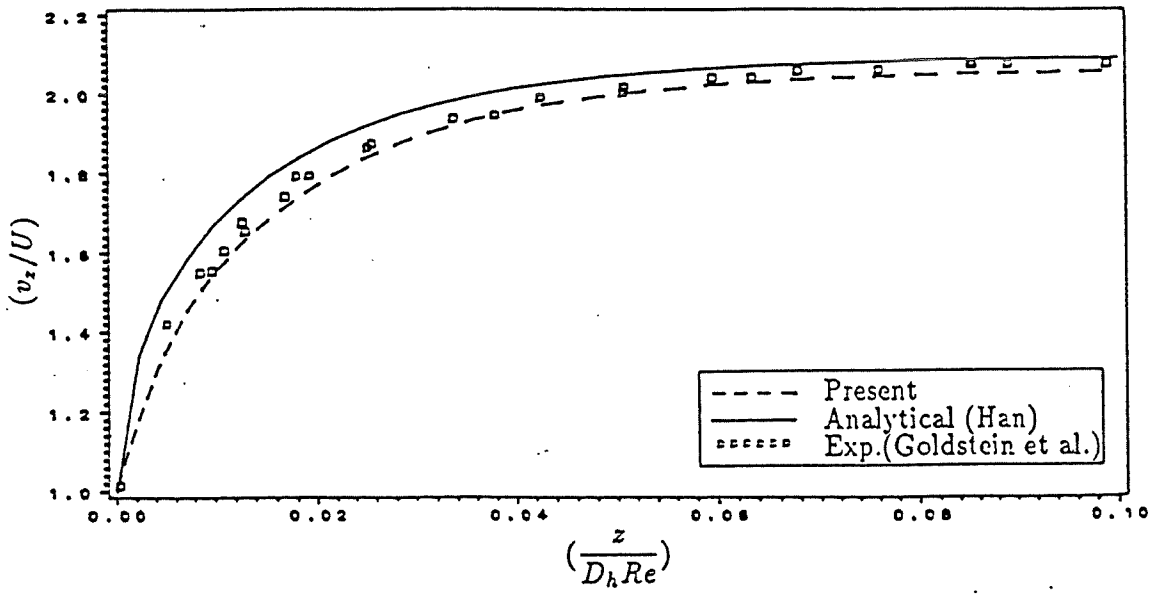

Figure 4: Center-Line Velocity Development, $\gamma = 1.0$

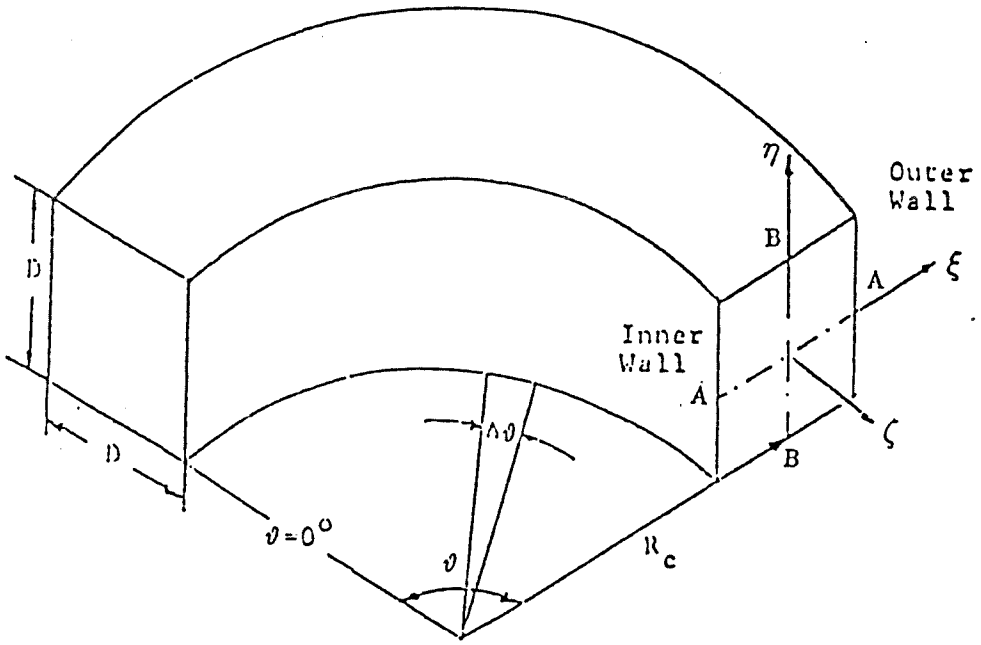

Figure 5: Square Curved Duct

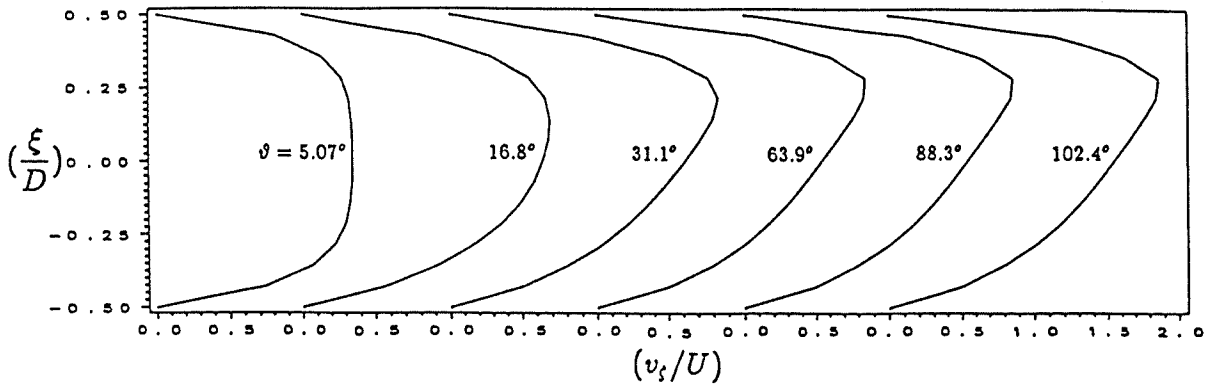

(a) Profile along A-A

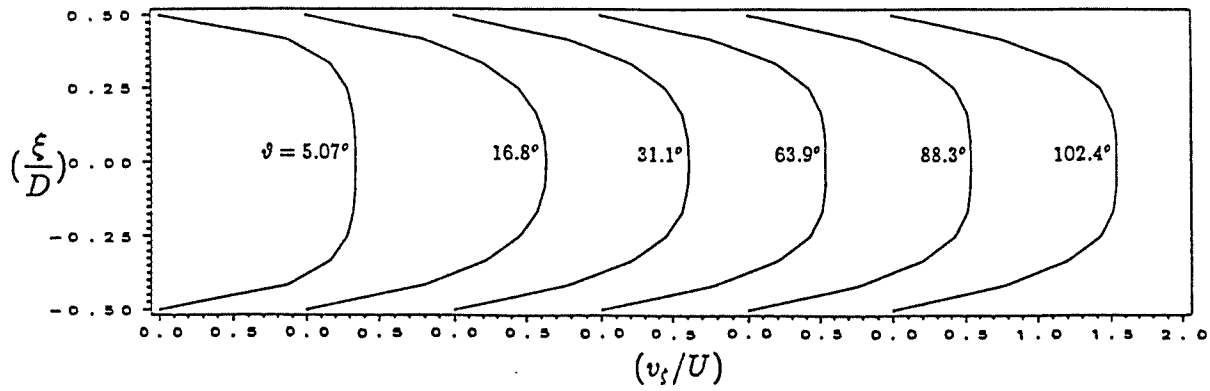

(b) Profile along B-B

Figure 6: Streamwise Velocity Development

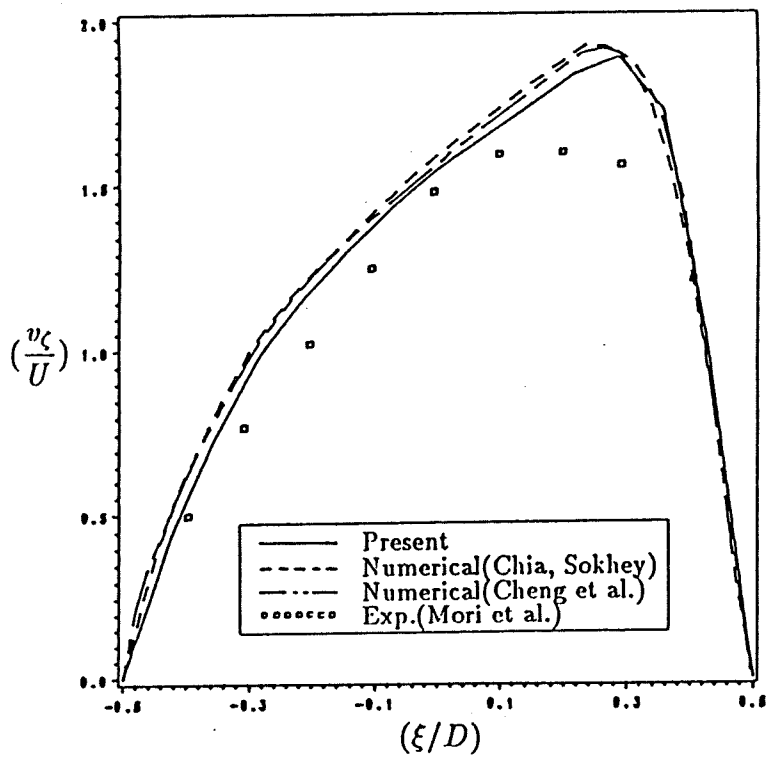

(a) Profile along A-A

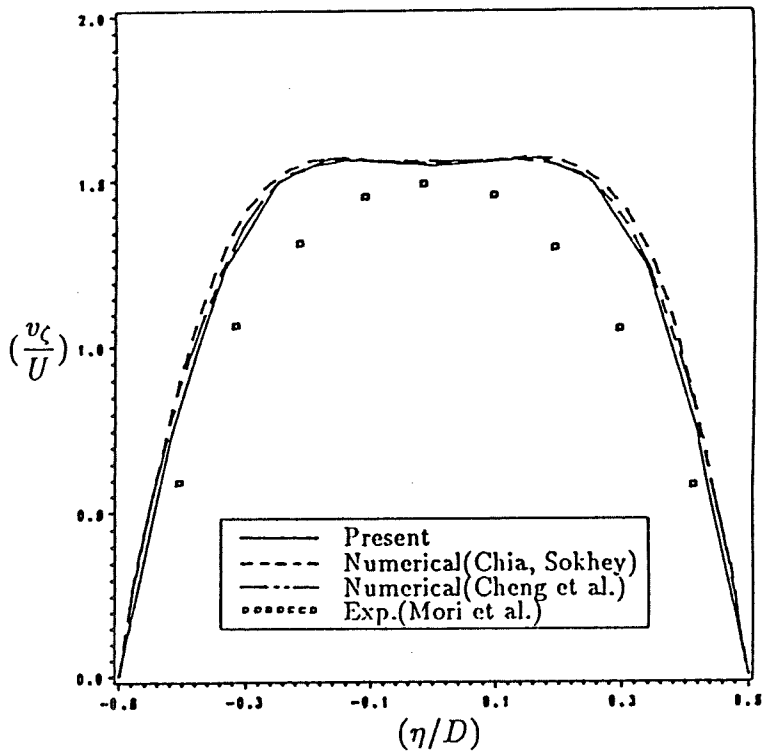

(b) Profile along B-B

Figure 7: Fully Developed Velocity, $\vartheta = 102.4^0$

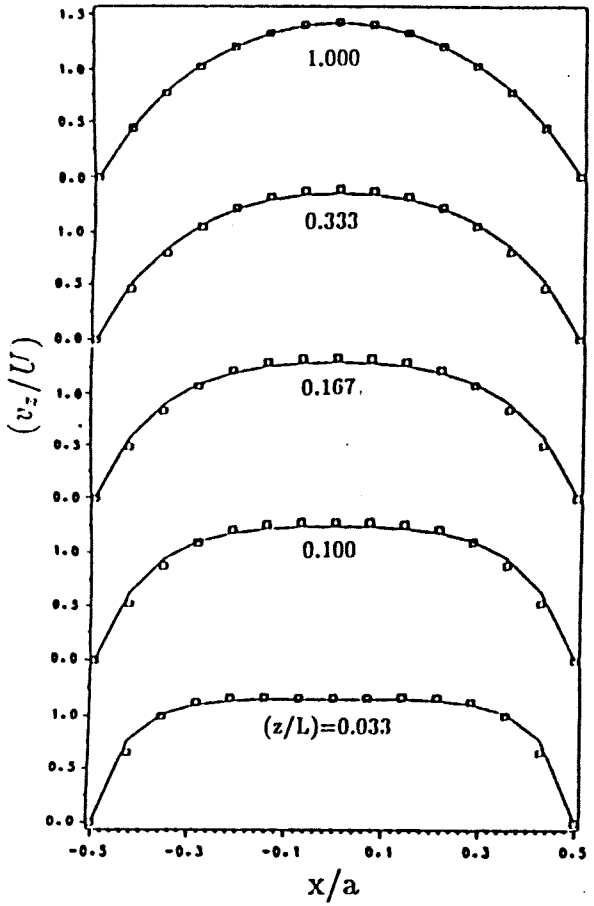

(a) $\gamma = 1.0$

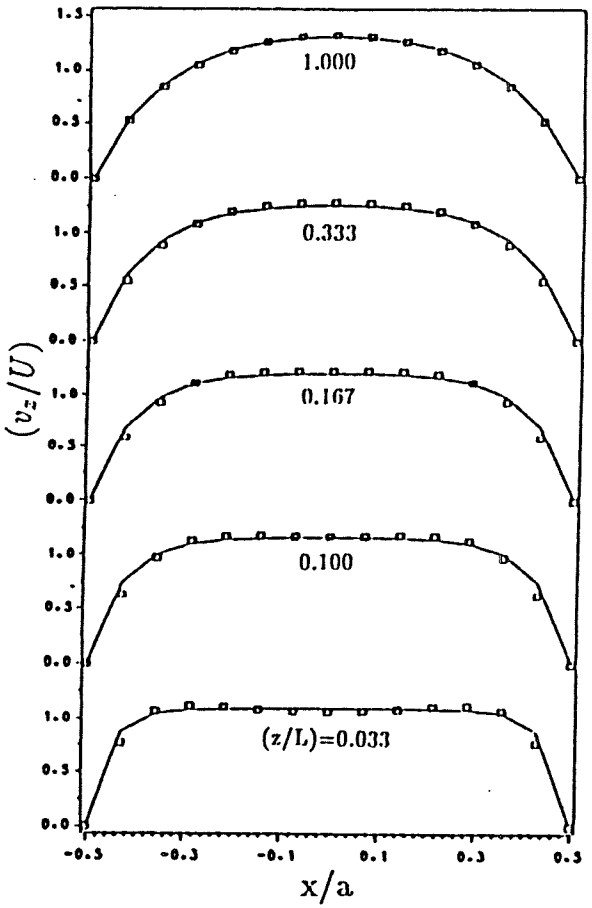

(b) $\gamma = 0.5$

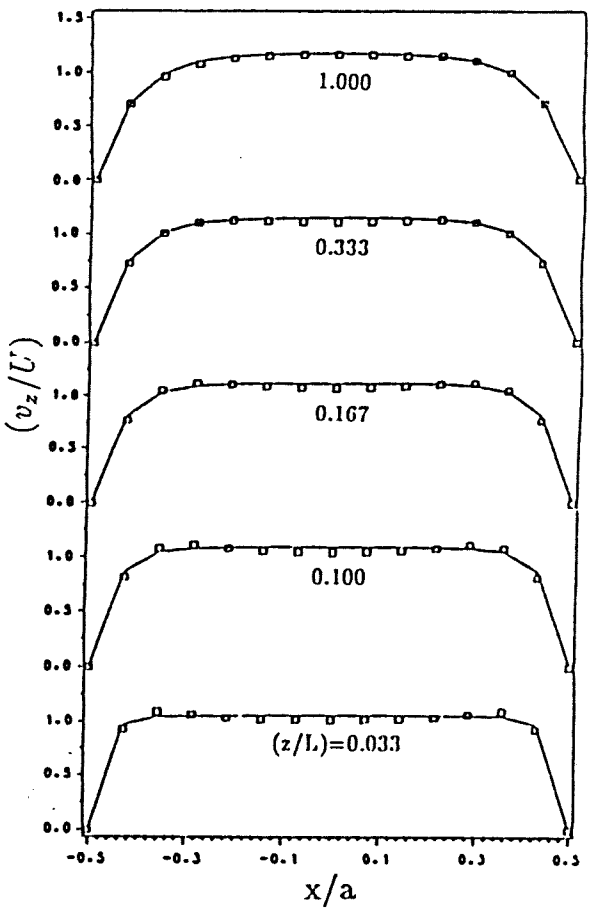

(c) $\gamma = 0.25$

Figure 8: Passage-Averaged Axial Velocity Profiles

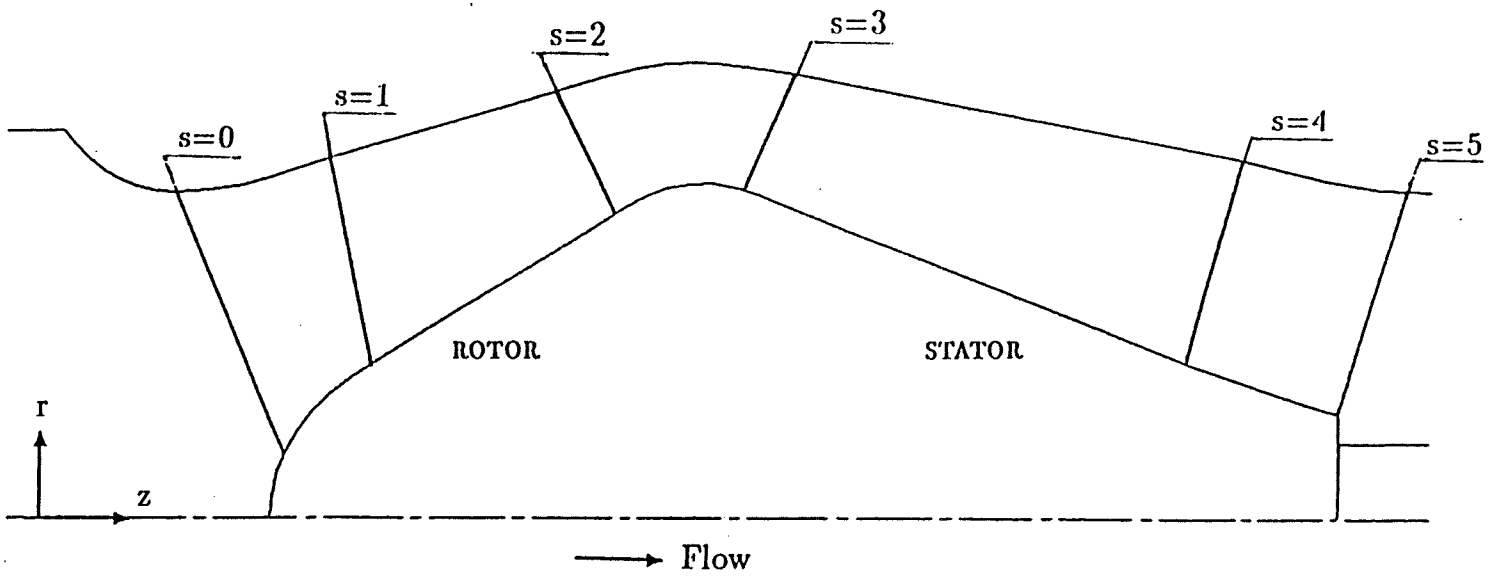

Figure 9: Domain for the MPAGE Computation

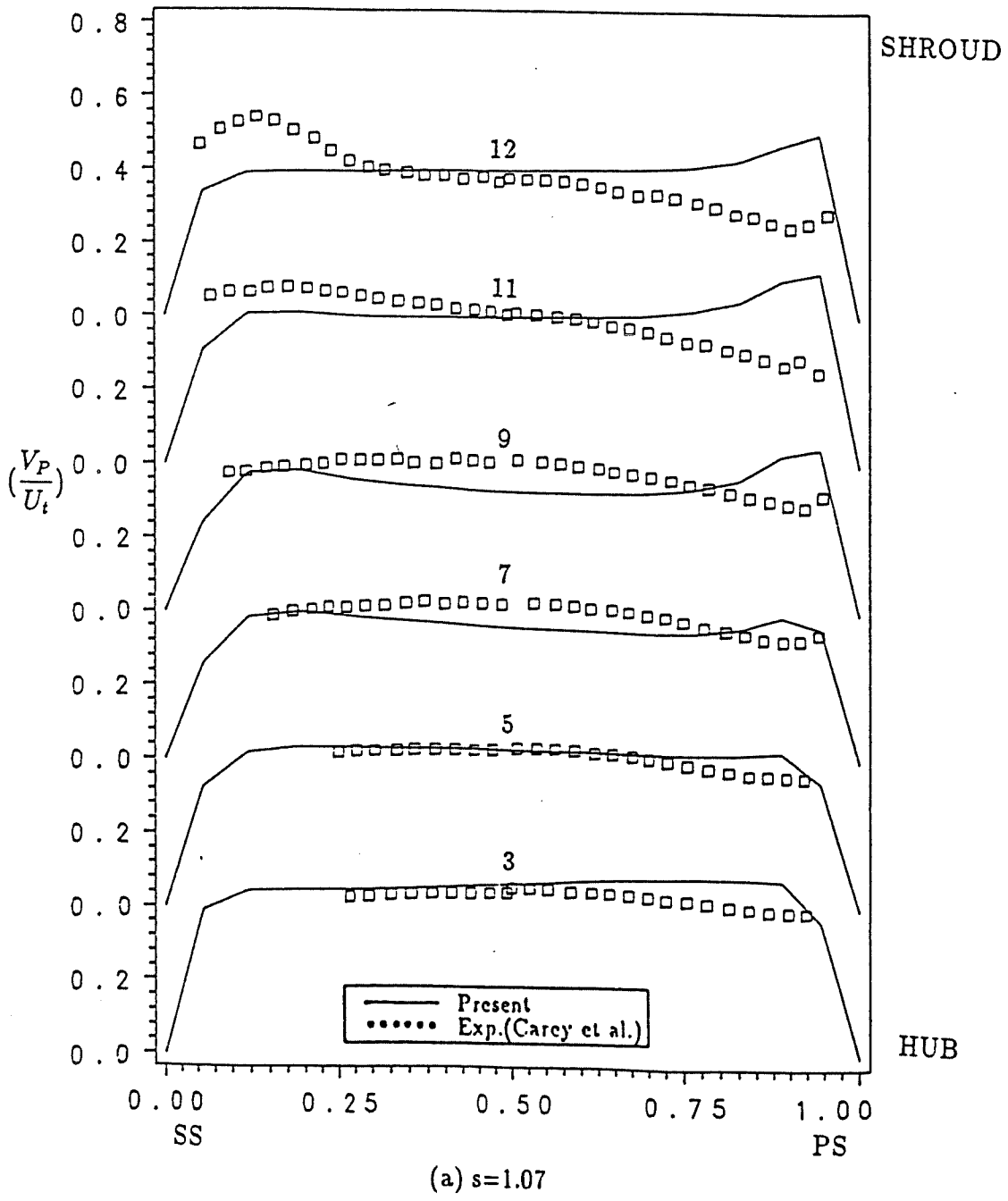

(a) s=1.07

Figure 10: Blade-to-Blade Velocity Components V_p, Rotor

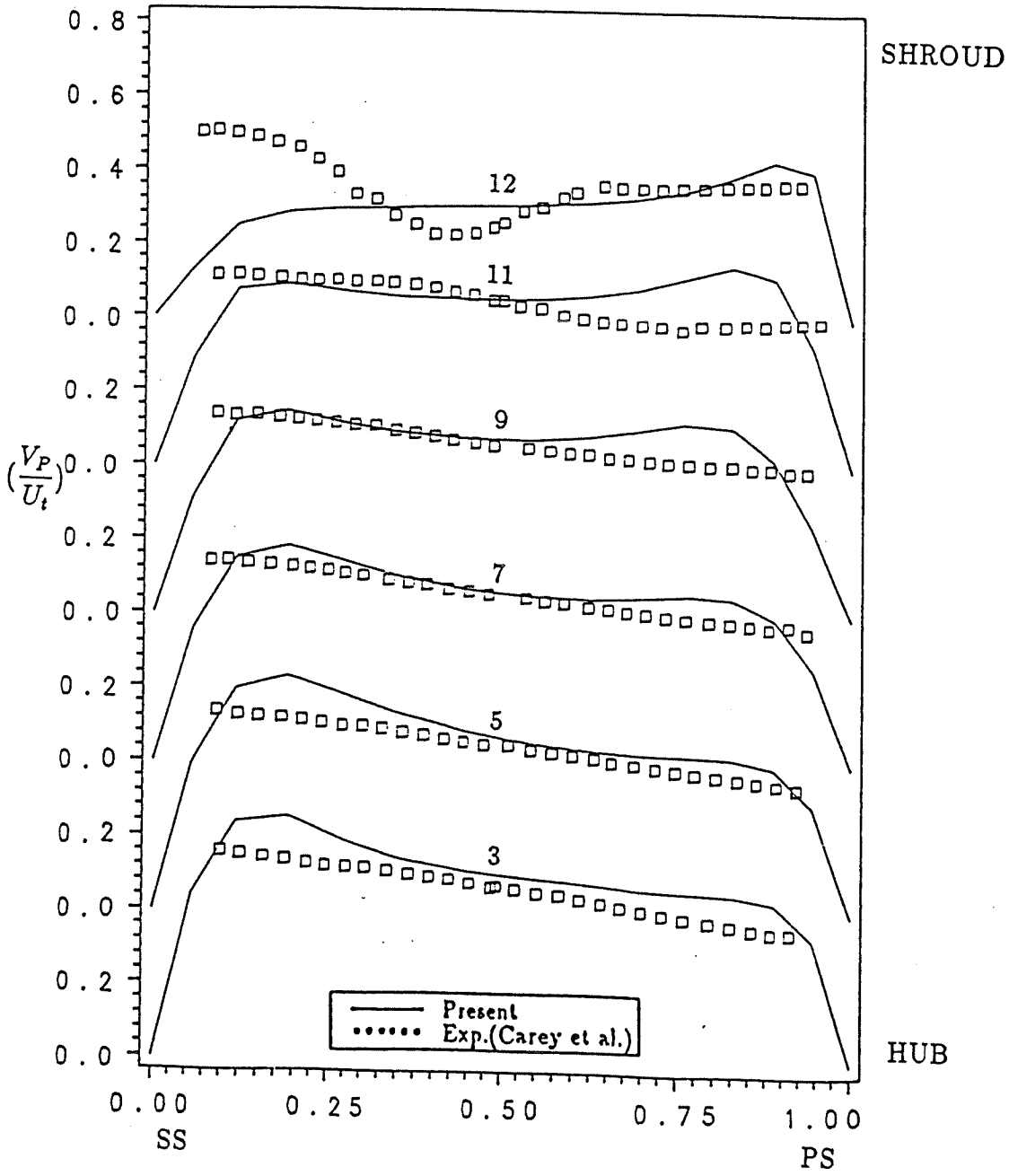

(b) s=1.50

Figure 10: Blade-to-Blade Velocity Components V_p, Rotor

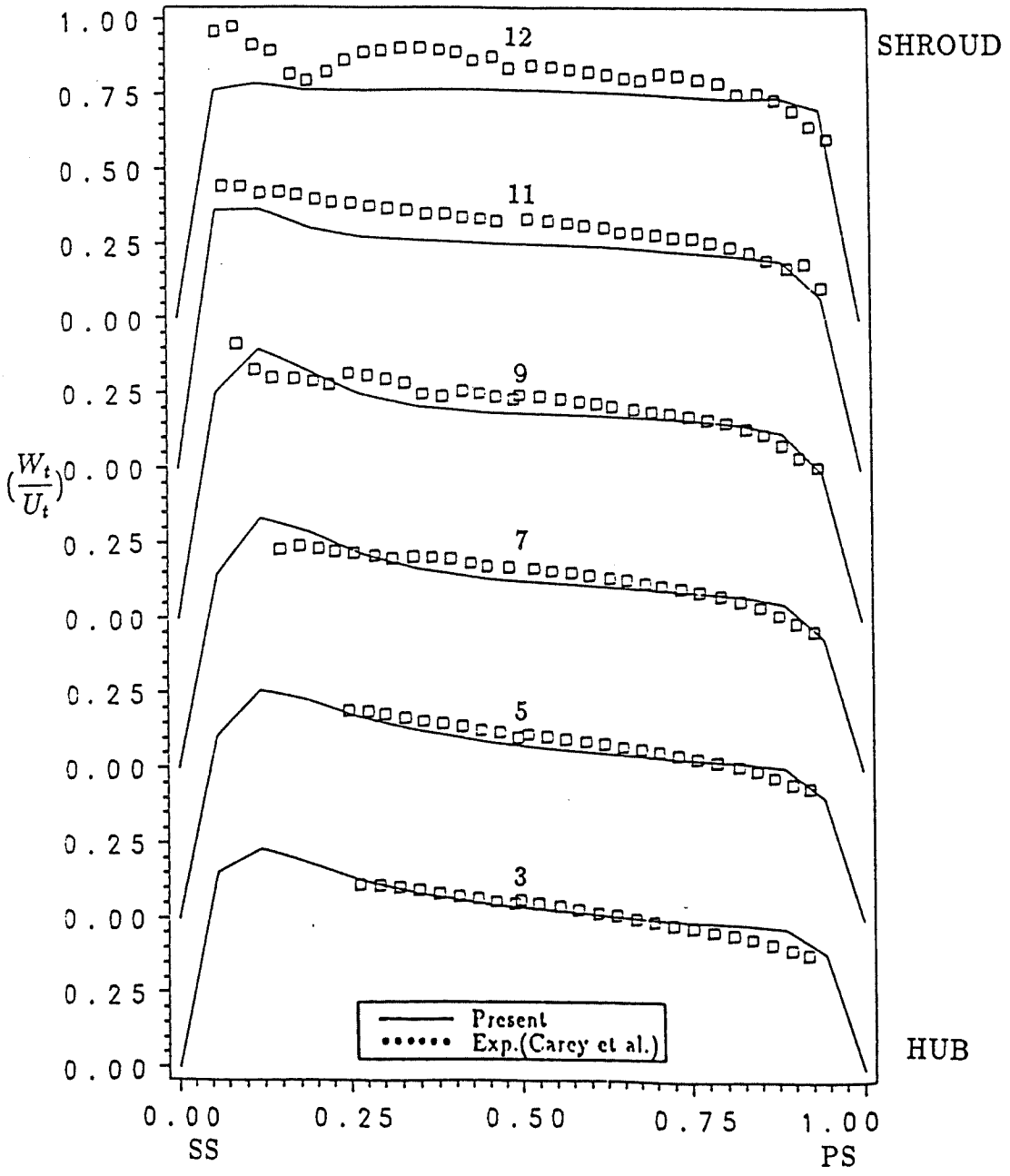

(a) s=1.07

Figure 11: Blade-to-Blade Velocity Components W_t, Rotor

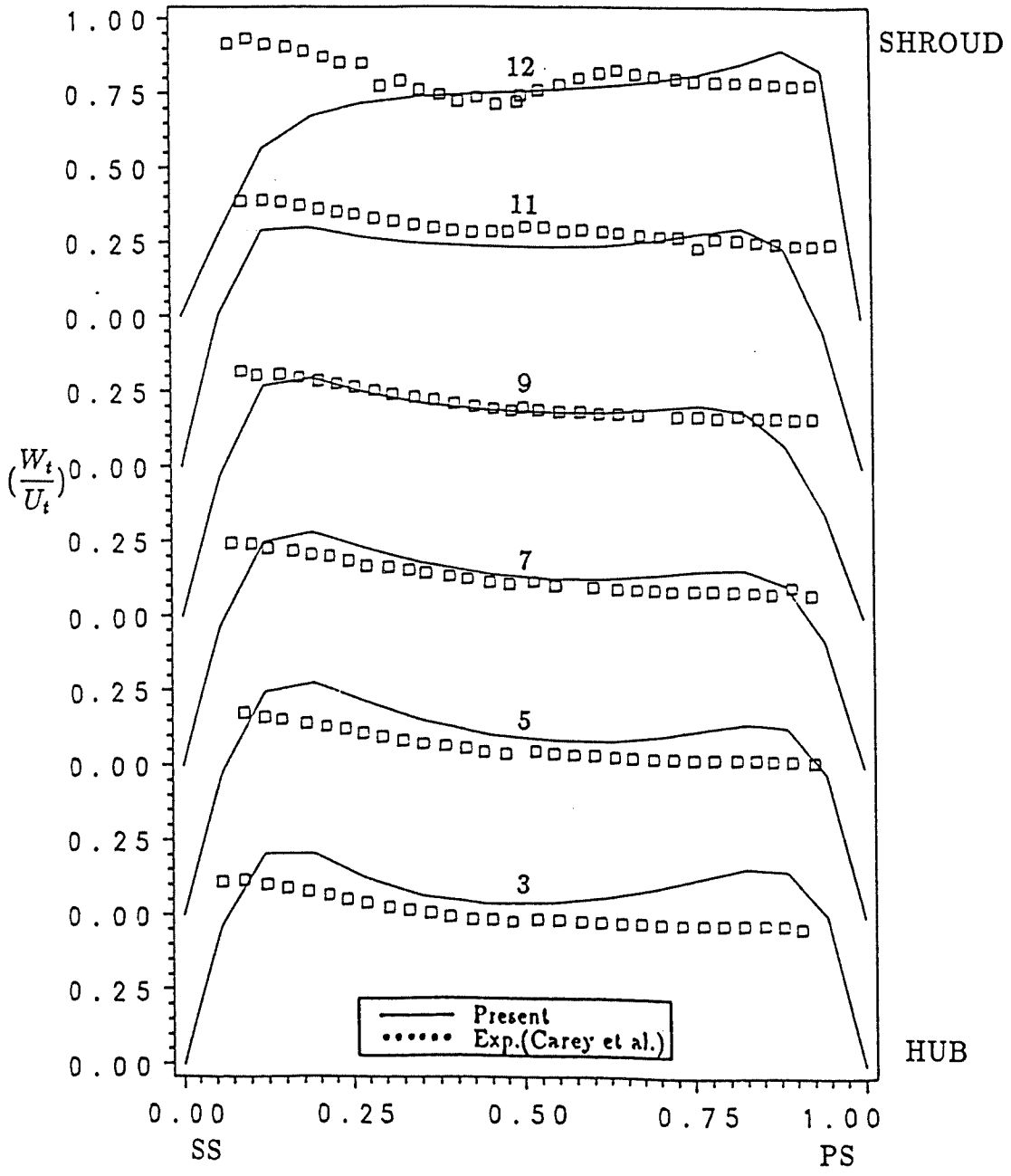

(b) s=1.50

Figure 11: Blade-to-Blade Velocity Components W_t, Rotor

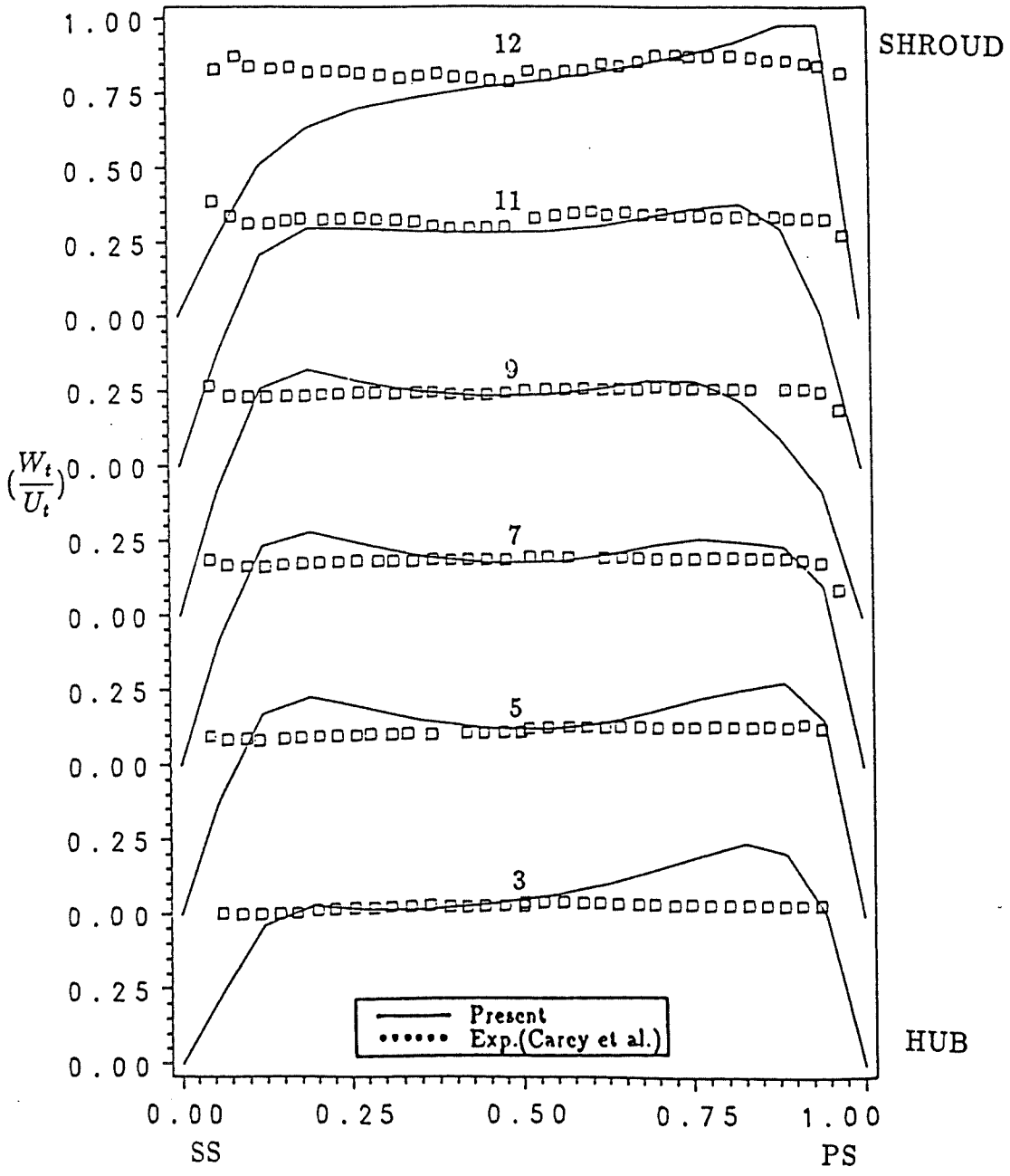

(c) s=1.86

Figure 11: Blade-to-Blade Velocity Components W_t, Rotor

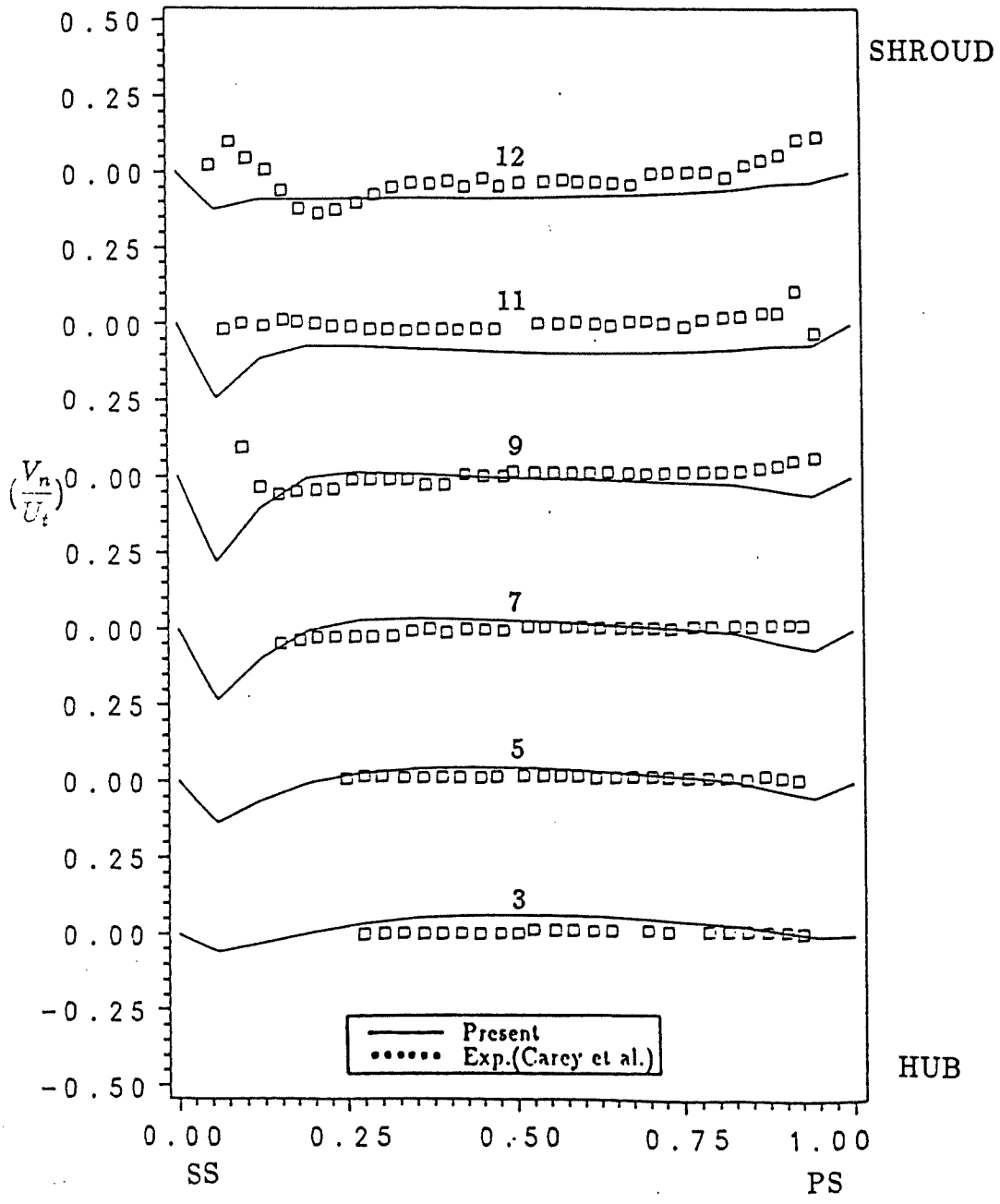

(a) s=1.07

Figure 12: Blade-to-Blade Velocity Components V_n, Rotor

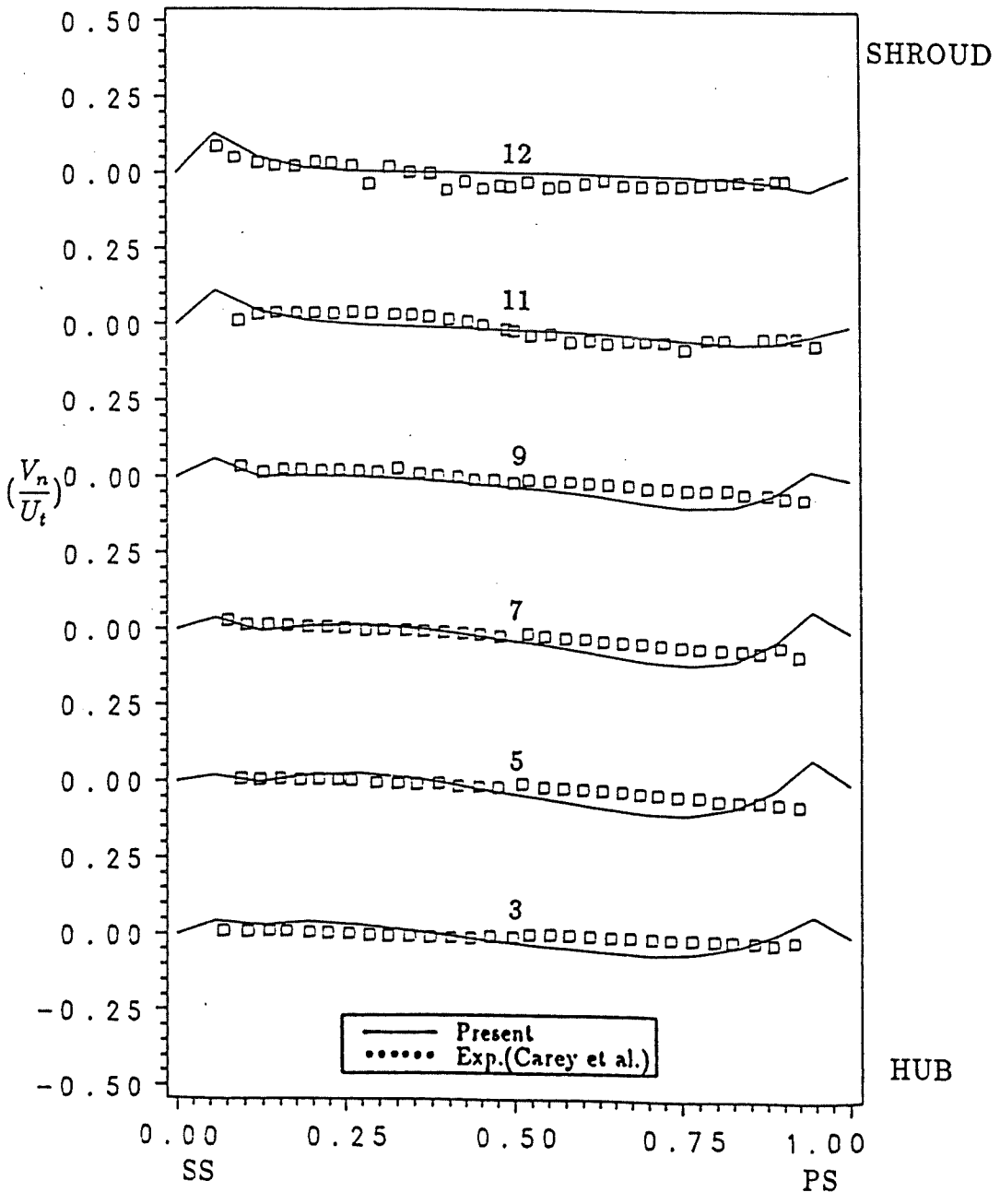

(b) s=1.50

Figure 12: Blade-to-Blade Velocity Components V_n, Rotor

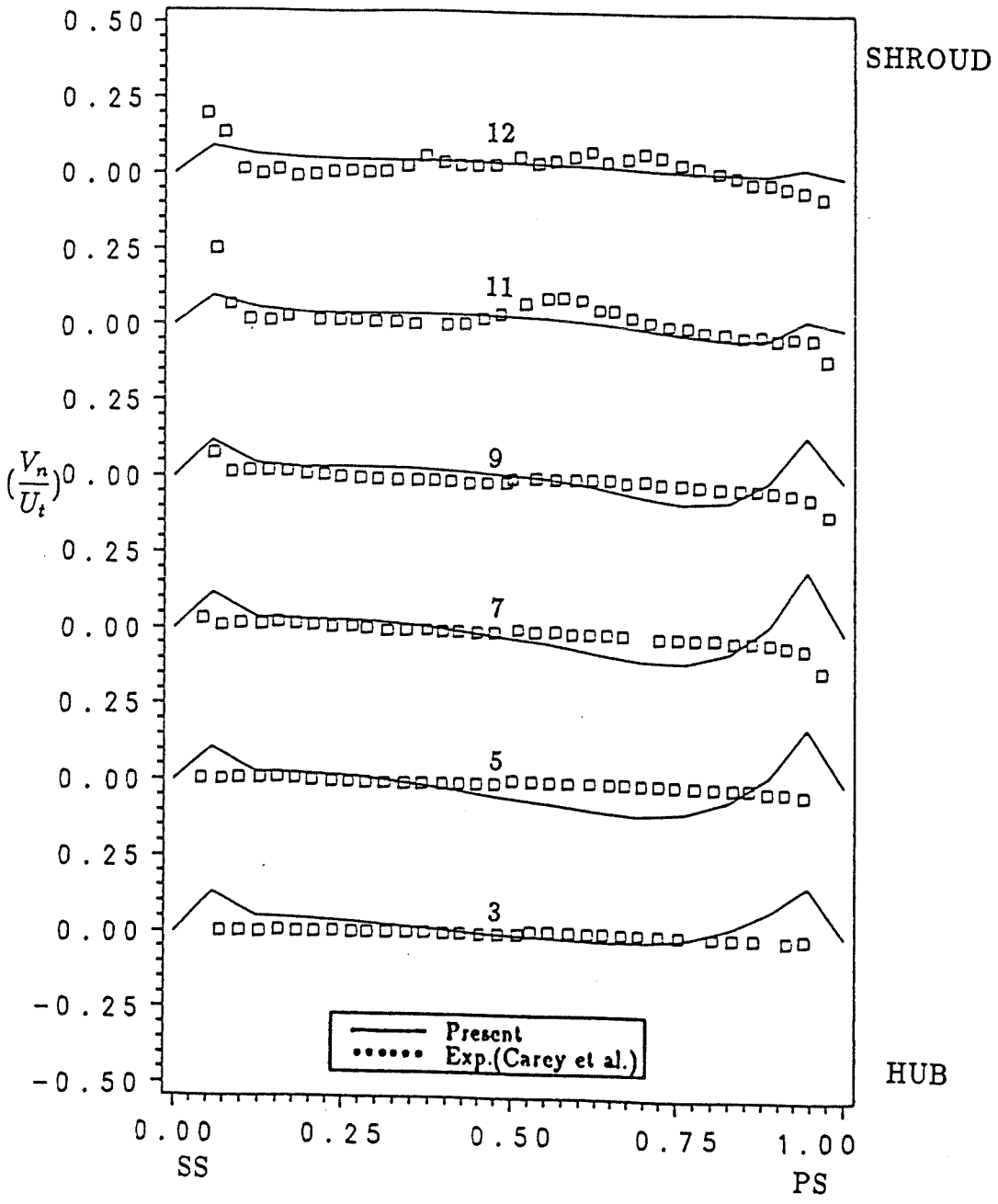

(c) s=1.86

Figure 12: Blade-to-Blade Velocity Components V_n, Rotor

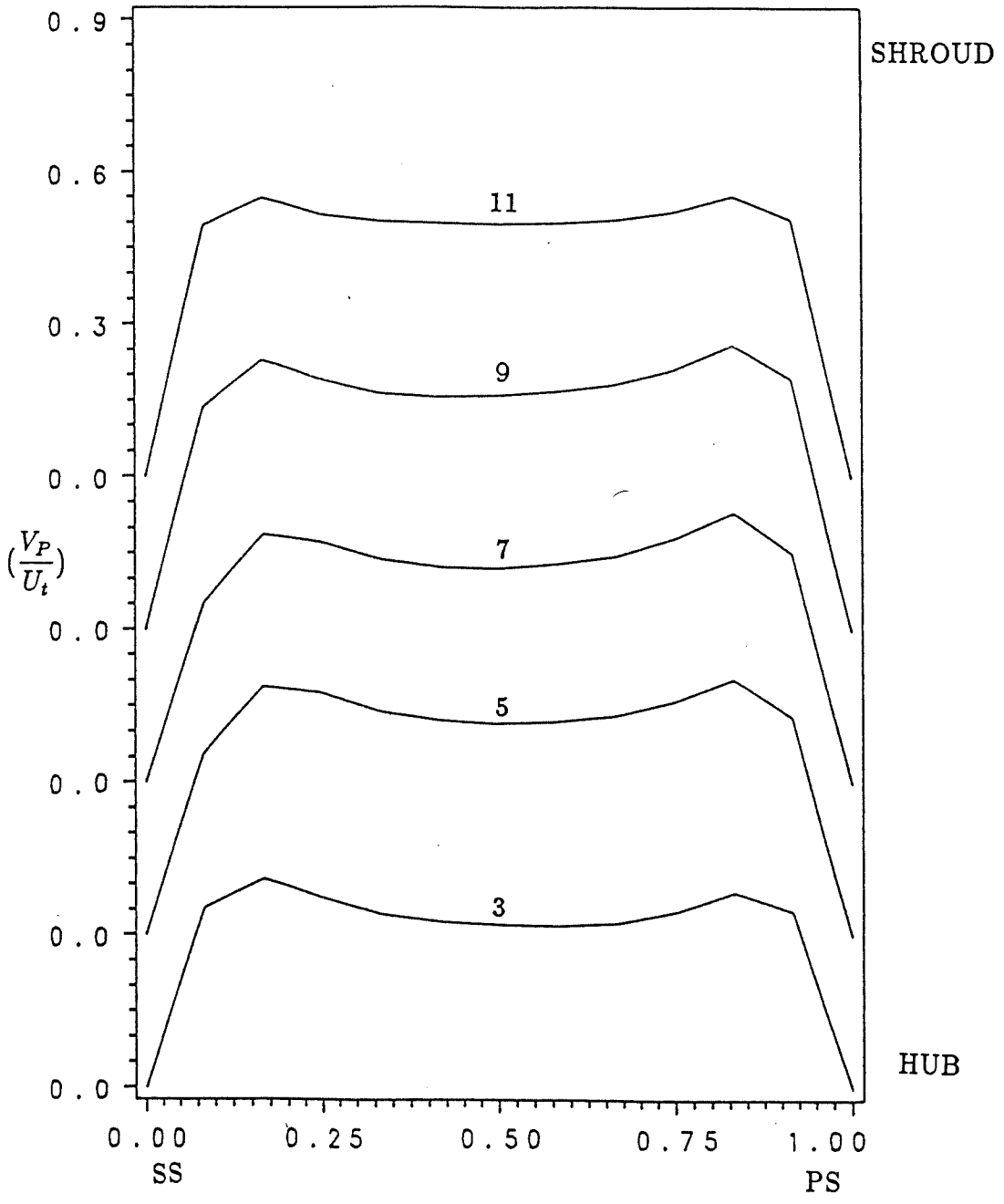

(a) s=3.1

Figure 13: Blade-to-Blade Velocity Component V_p, Stator

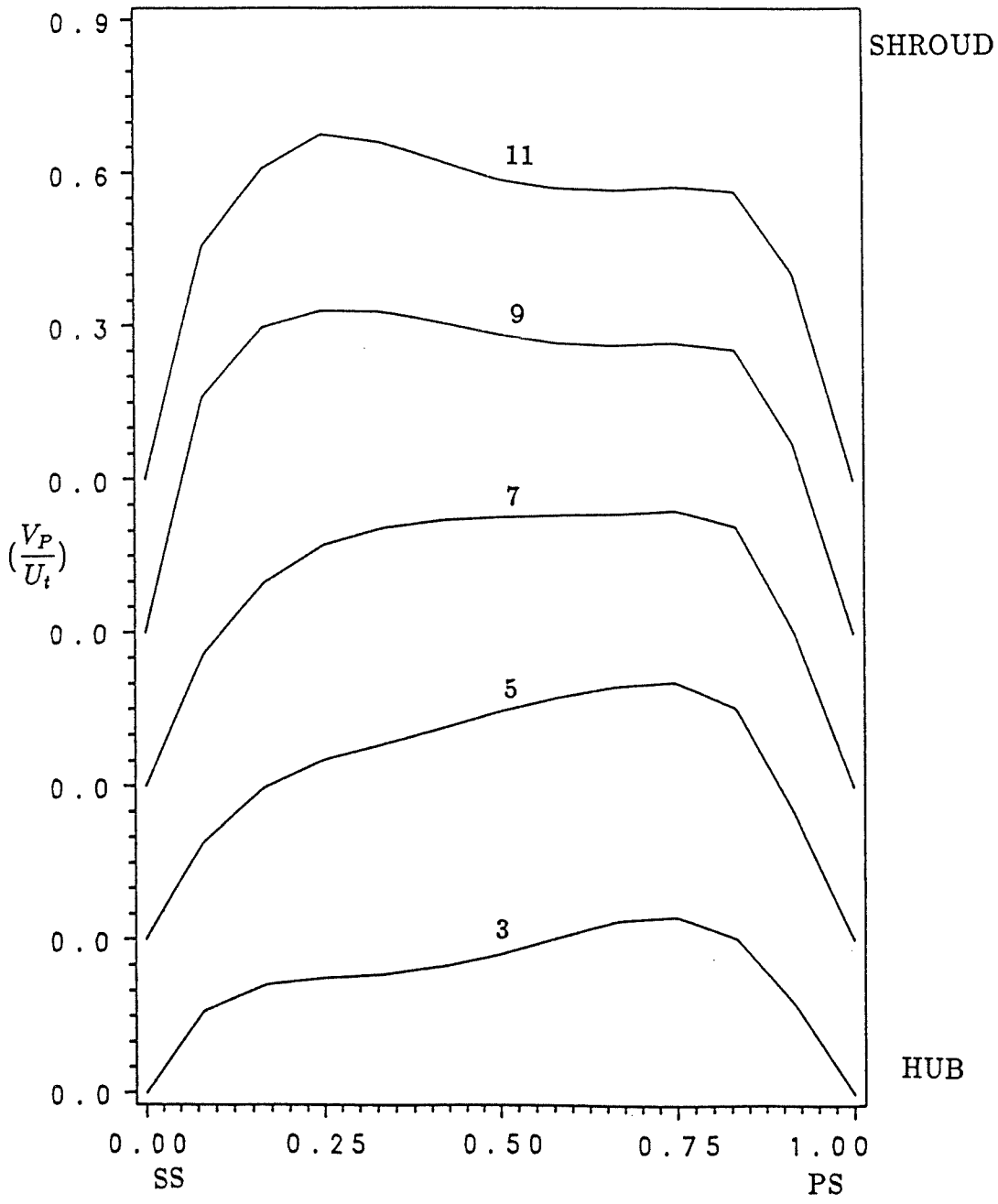

(b) s=3.5

Figure 13: Blade-to-Blade Velocity Component V_p, Stator

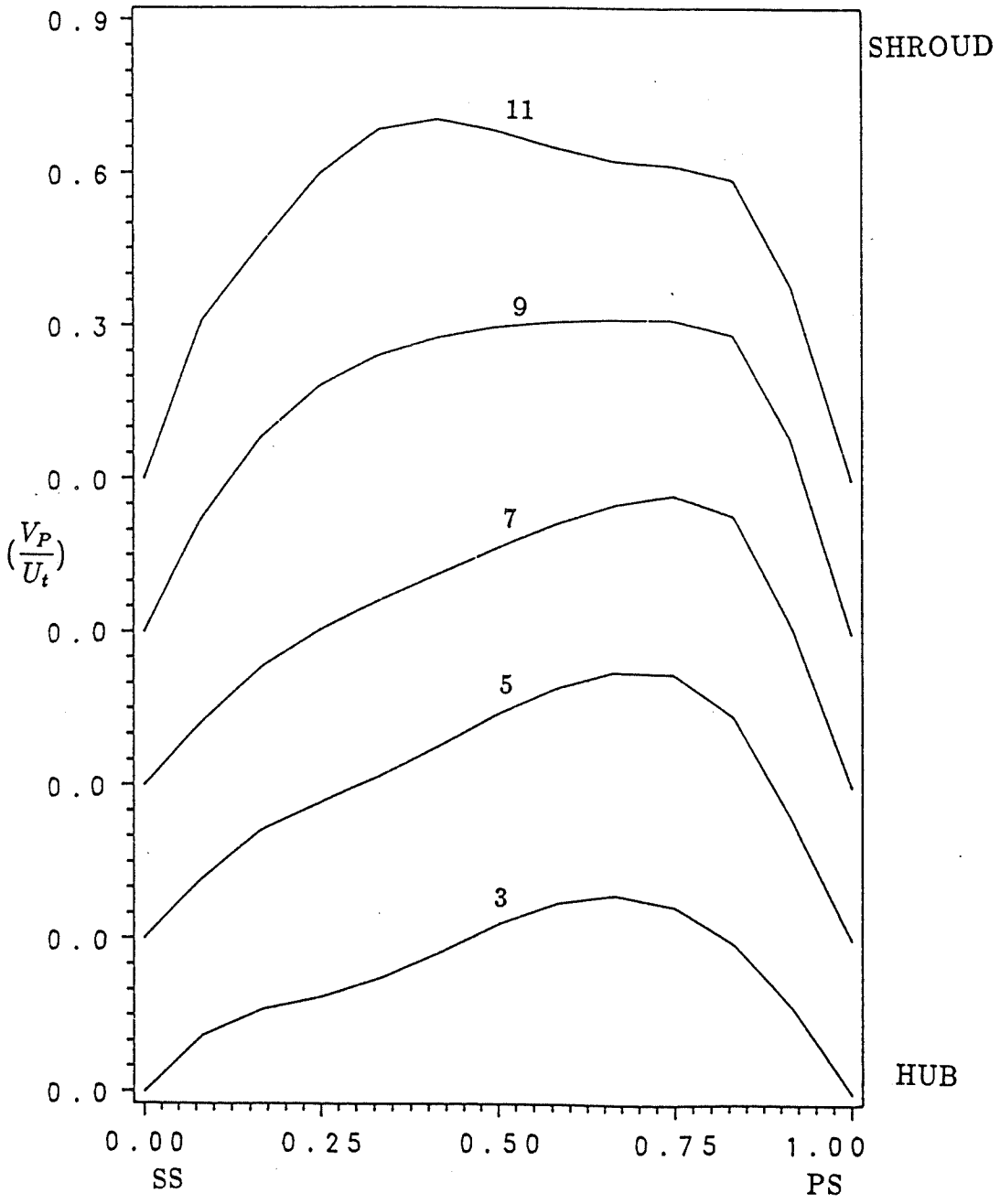

(c) s=3.9

Figure 13: Blade-to-Blade Velocity Component V_p, Stator

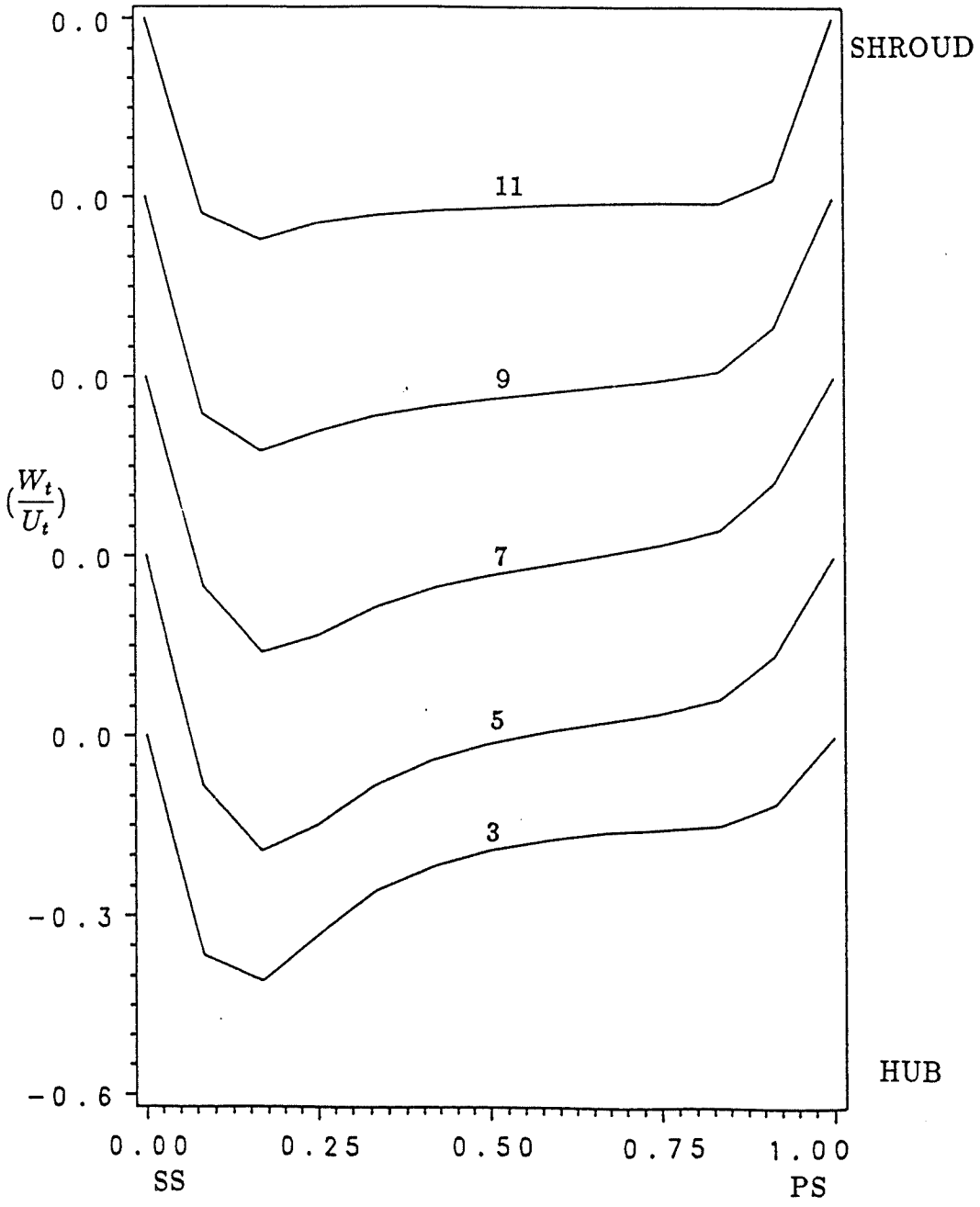

(a) s=3.1

Figure 14: Blade-to-Blade Velocity Component V_t, Stator

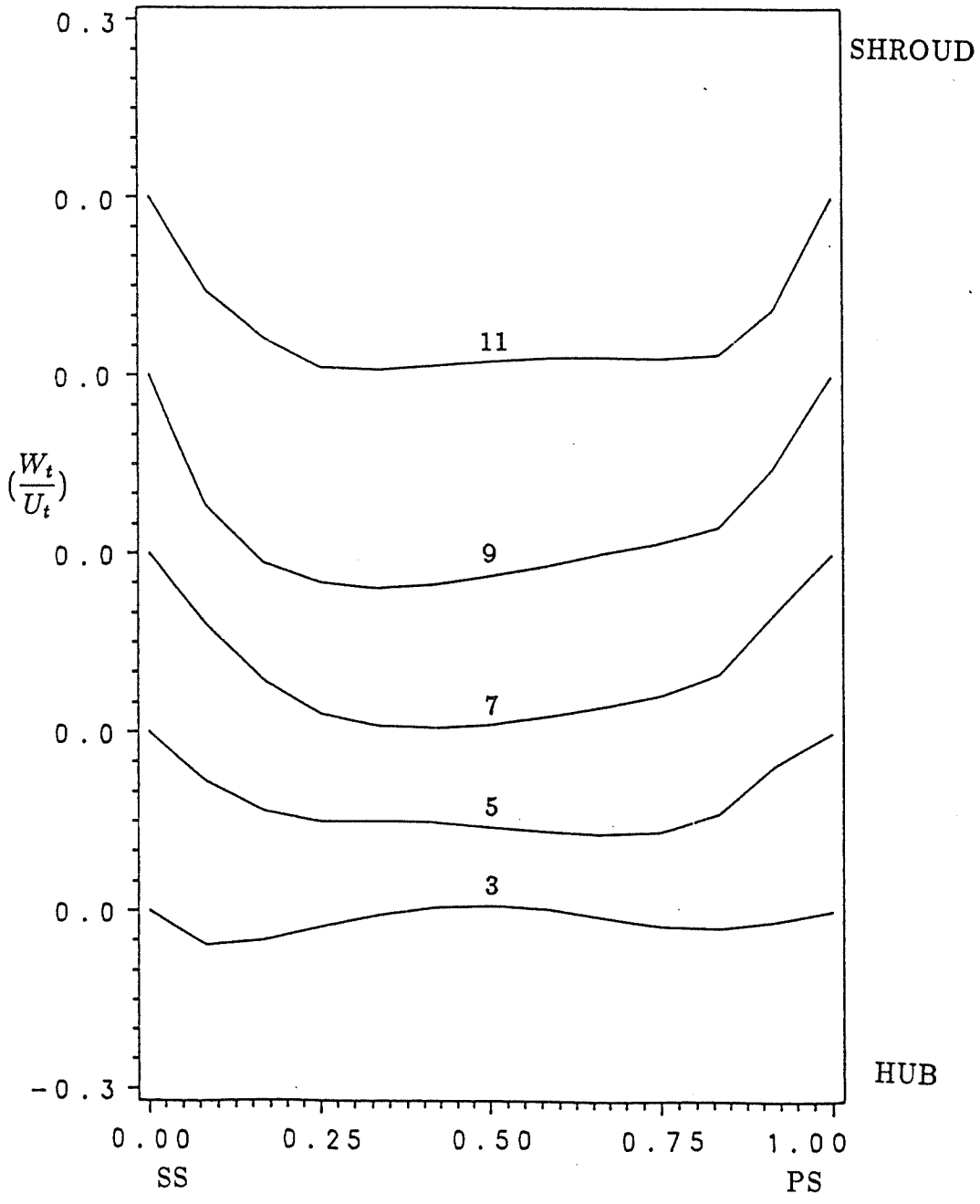

(b) s=3.5

Figure 14: Blade-to-Blade Velocity Component V_t, Stator

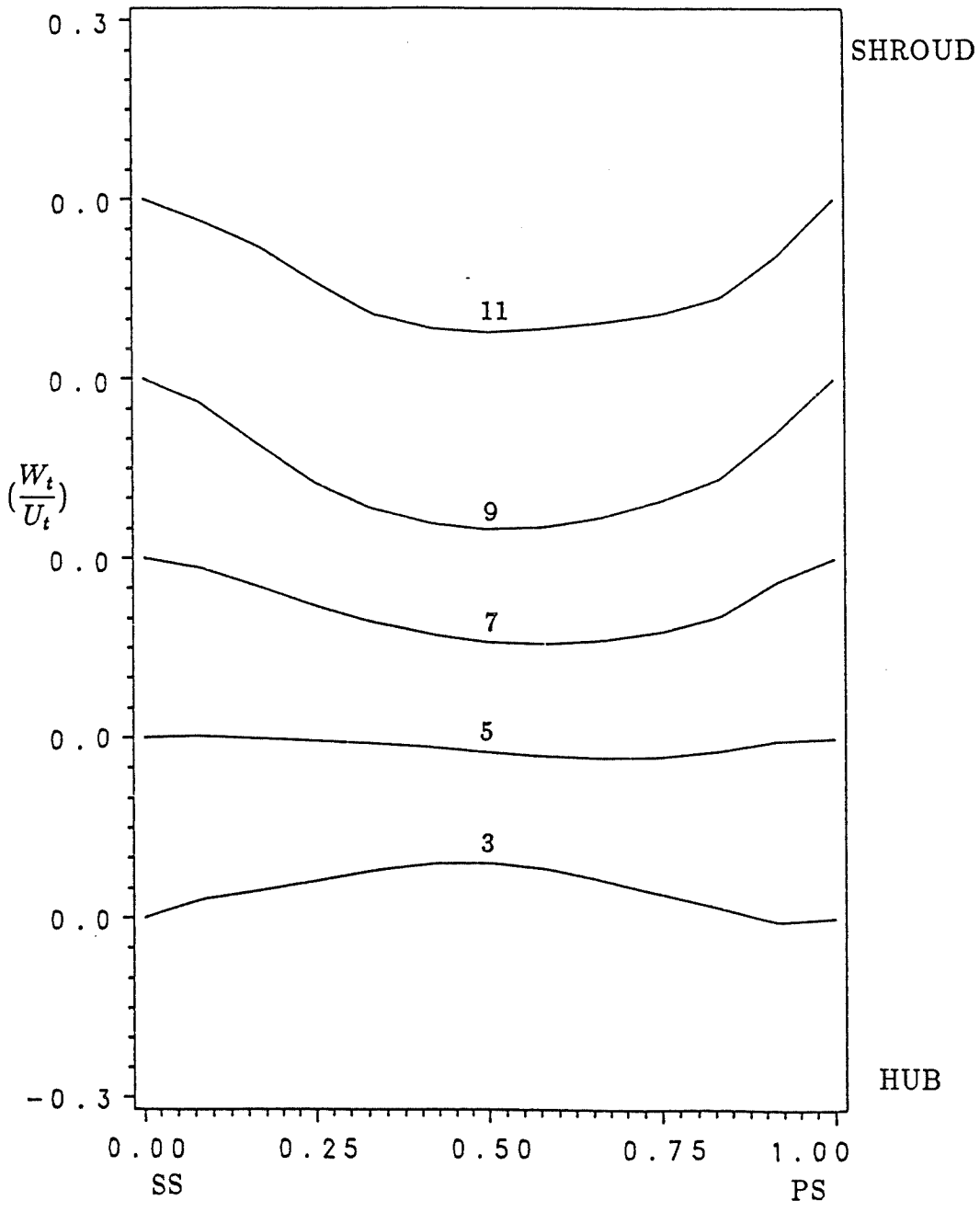

(c) s=3.9

Figure 14: Blade-to-Blade Velocity Component V_t, Stator

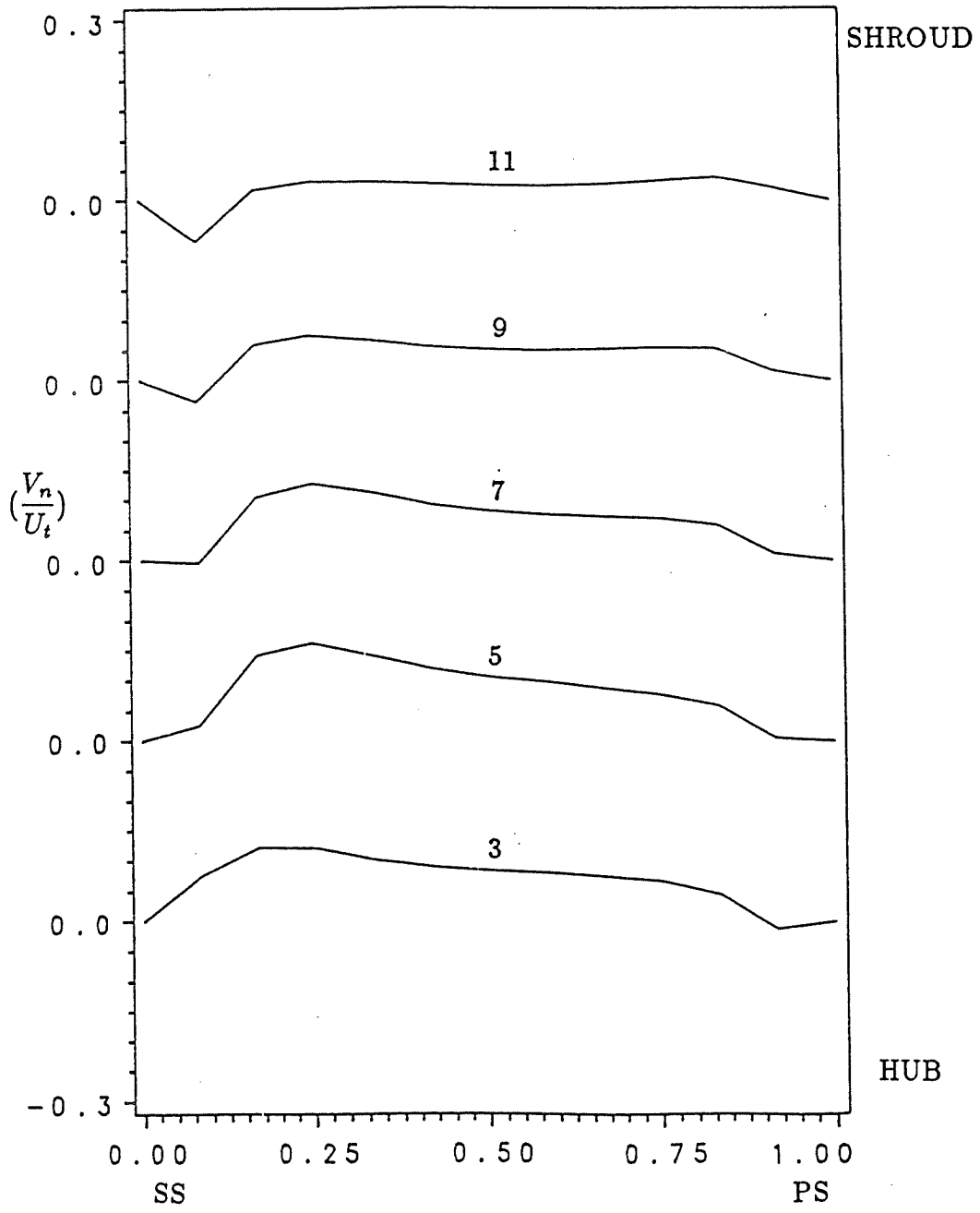

(a) s=3.1

Figure 15: Blade-to-Blade Velocity Component V_n, Stator

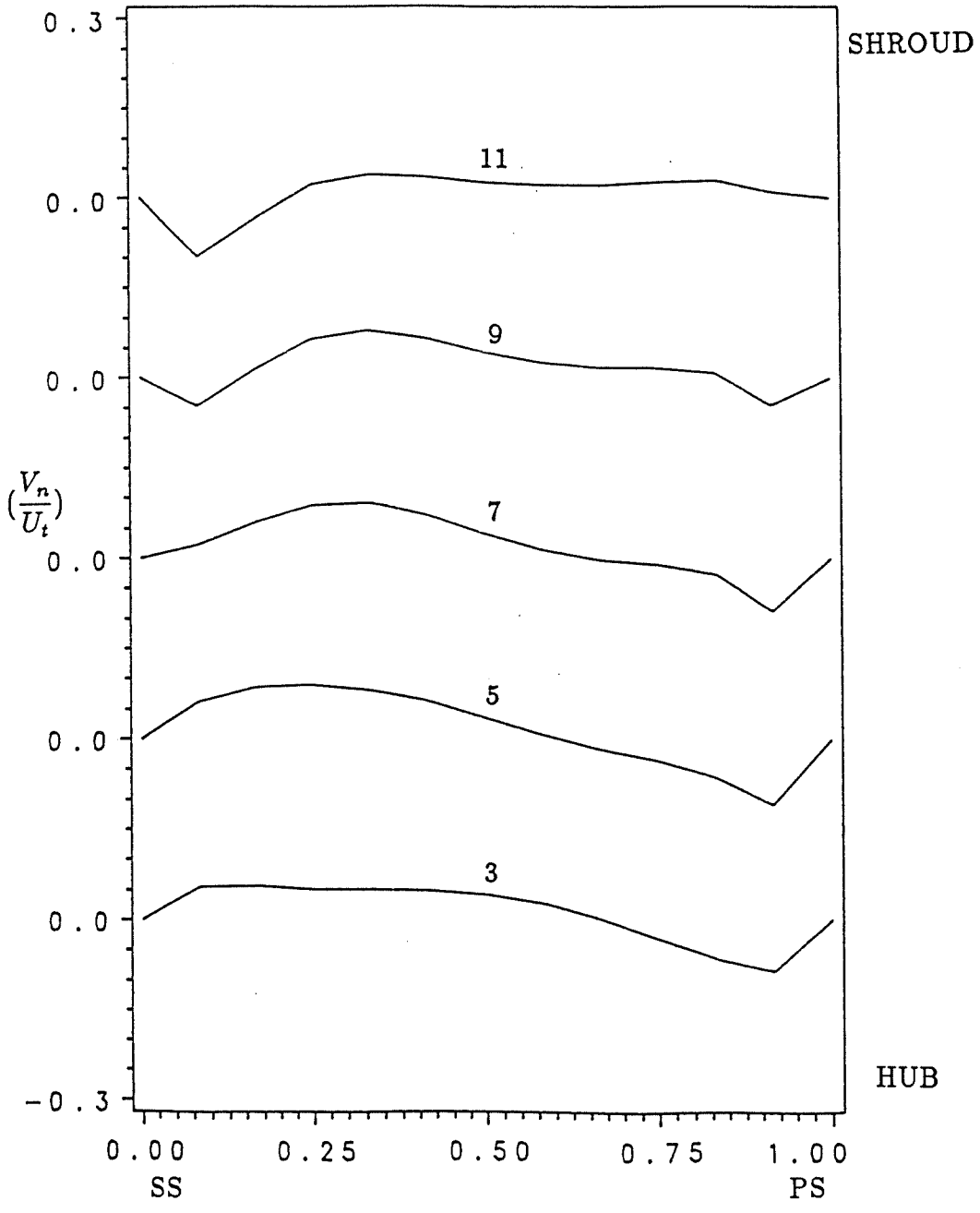

(b) s=3.5

Figure 15: Blade-to-Blade Velocity Component V_n, Stator

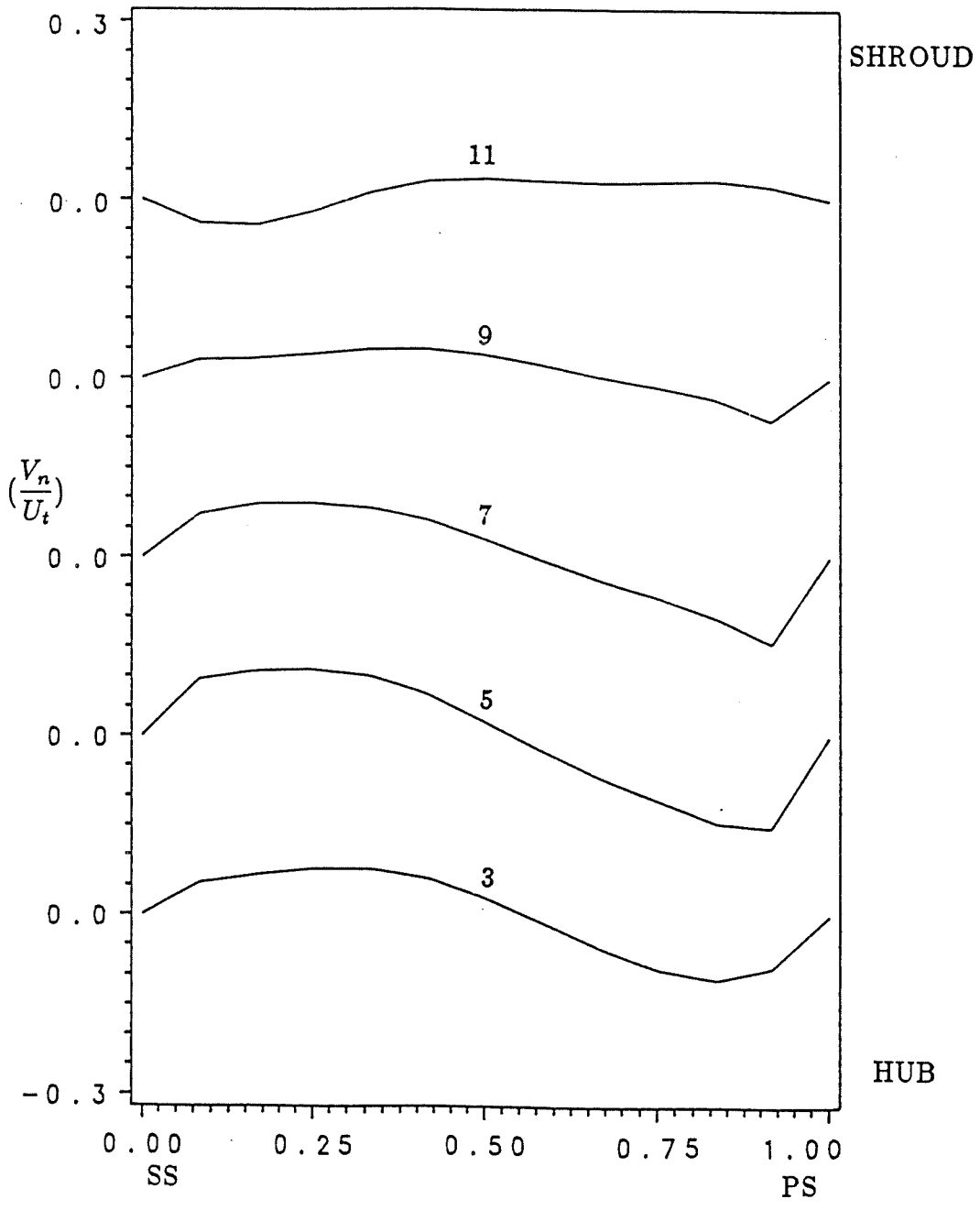

(c) s=3.9

Figure 15: Blade-to-Blade Velocity Component V_n, Stator

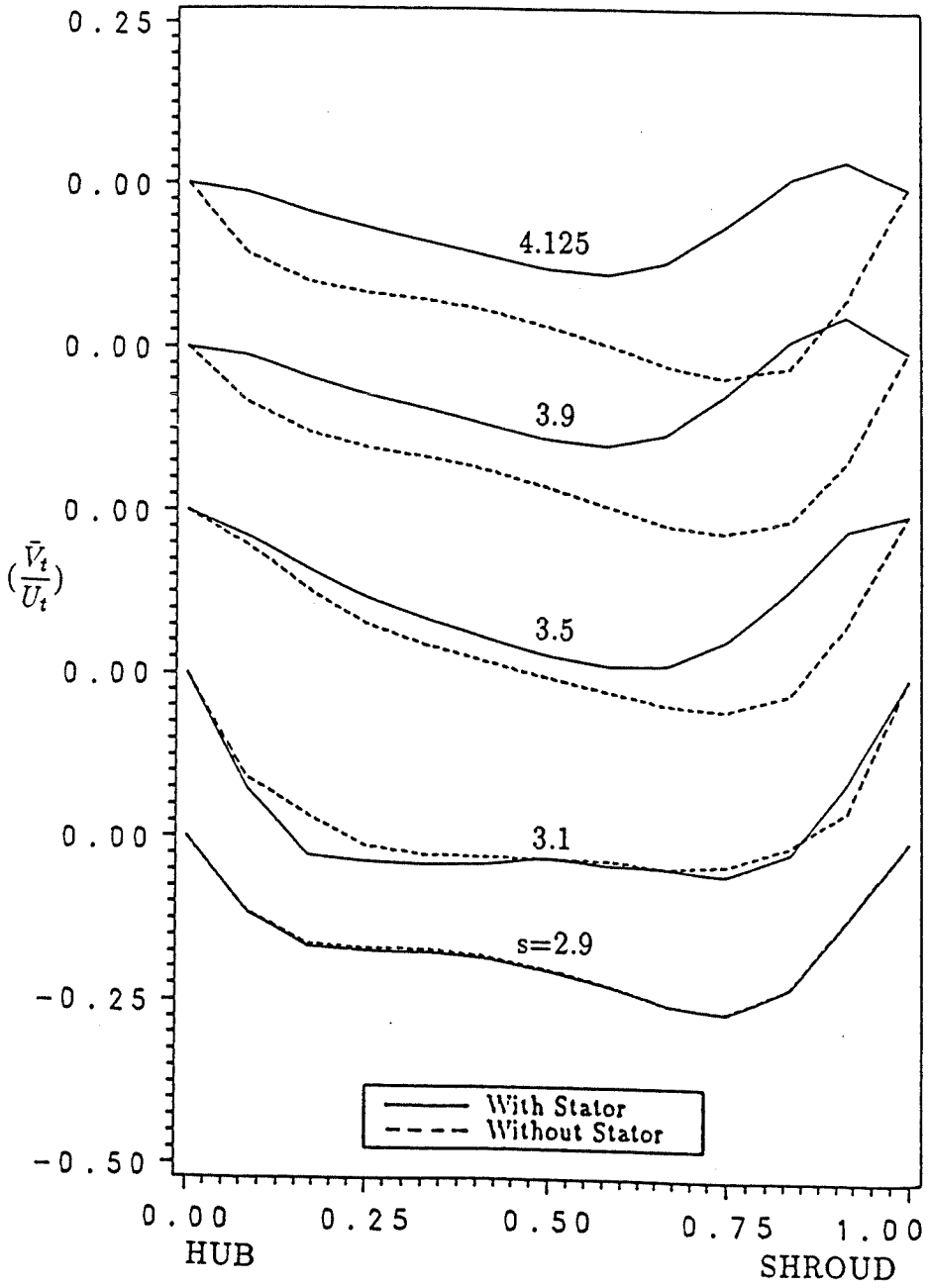

(b) Component $\bar{V}_t$

Figure 16: Passage-Averaged Hub-to-Shroud Velocities with and without the Stator